Energy & Buildings 359 (2026) 117281

Contents lists available at ScienceDirect

Energy & Buildings

journal homepage: www.elsevier.com/locate/enb

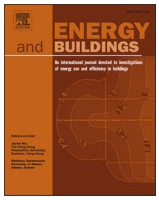

Dynamic real-time control for a multi-energy prosumer with electricity and heat

Pablo Horrillo-Quintero [a], Pablo García-Triviño [b], Carlos E. Ugalde-Loo [c], David Carrasco-González [b], Vedran Peric [d], Luis M. Fernández-Ramírez [b,*]

[a] Research Group in Sustainable and Renewable Electrical Technologies (PAIDI-TEP023), Department of Electrical Engineering, ESI Puerto Real, University of Cadiz, Avda. Universidad de Cadiz, no 10, 11519 Puerto Real (Cadiz), Spain
[b] Research Group in Sustainable and Renewable Electrical Technologies (PAIDI-TEP023), Department of Electrical Engineering, Higher Technical School of Engineering of Algeciras (ETSIA), University of Cadiz, Avda. Ramón Puyol, s/n. 11202 Algeciras (Cadiz), Spain
[c] School of Engineering, Cardiff University, Cardiff CF24 3AA, UK
[d] Chair of Intelligent Energy Management, University of Bayreuth 95448 Bayreuth, Germany

ARTICLE INFO

Keywords:
Multi-energy prosumer
Dynamic real-time control
Electricity
Heating
Energy management system

ABSTRACT

Multi-energy prosumers have emerged as a promising avenue for curtailing energy consumption by integrating diverse energy vectors in a synchronised operation. Prevailing investigations have predominantly focused on static analyses directed at optimising cost functions for power dispatch problems, often overlooking the dynamic facets of the system. This paper introduces a dynamic real-time control scheme for a multi-energy prosumer encompassing electricity and heat as energy vectors. A novel state-based energy management system (EMS) is designed, with the goal of ensuring energy balance (electrical and thermal), while prioritising the utilization of renewable energy and diminishing reliance on local electrical distribution networks. To this end, three different operating modes are defined regarding the real-time renewable capacity. The EMS and multi-energy prosumer are subjected to evaluation across several weather conditions in a 4-h variable load profile. A sensibility analysis considering 250 simulations of 1-h duration, with a wide range of irradiance, water demand, underfloor heating load, and state-of-charge conditions were used to validate the control response, demonstrating the lack of use of the local grid. Moreover, a real-time experiment employing hardware-in-the-loop testing with an OPAL-RT4512 unit and a dSPACE MicroLabBox control prototype confirms the adequate response in a practical scenario. Comparative validation against a fuzzy-logic benchmark throughout a 24-h dynamic horizon revealed that the proposed state-based EMS reduced grid dependency by 36.61% and auxiliary gas boiler by 2.23%. Furthermore, the architecture achieved a 30-fold reduction in computational time while maintaining negligible control errors, establishing its superior suitability for real-time implementation in prosumers environments.

1. Introduction

The pursuit to improve energy efficiency in towns and industries by combining electricity and heat demand is propelling the advancement of distributed power generation employing multi-energy prosumers based on renewable electrical technologies (RETs) [1]. The extensive incorporation of various energy sources and loads in contemporary distribution grids is an unavoidable fact in the forthcoming evolution of energy systems [2].

Suboptimal energy utilisation factors, diminished overall efficiency, and compromised resilience often stem from the fragmented nature of energy system development. When strategic planning, engineering, and operational execution are decoupled for individual systems, the resulting lack of synchronisation inherently degrades the performance and self-healing capacity of the supply framework [3].

The modelling of multi-energy prosumers is typically approached from two distinct viewpoints: 'static' and 'dynamic'. The static paradigm is characterised by a stationary framework that employs predefined operational strategies, rendering it unresponsive to real-time fluctuations in energy demand [4–6]. These strategies usually rely on historical data or predefined rules. Traditionally, this approach considers long-time horizons to optimise an objective function [7]. The second

* Corresponding author.
E-mail addresses: pablo.horrillo@uca.es (P. Horrillo-Quintero), pablo.garcia@uca.es (P. García-Triviño), ugalde-looc@cardiff.ac.uk (C.E. Ugalde-Loo), david.carrasco@uca.es (D. Carrasco-González), vedran.peric@uni-bayreuth.de (V. Peric), luis.fernandez@uca.es (L.M. Fernández-Ramírez).

https://doi.org/10.1016/j.enbuild.2026.117281
Received 10 November 2025; Received in revised form 30 January 2026; Accepted 5 March 2026
Available online 9 March 2026

perspective focuses on real-time control and considers transient modes. It possesses the capability to promptly adapt to changes in demand, modifying production in response in meteorological parameters and the charge status (SOC) of the energy storage units (ESSs) [8,9]. Nevertheless, the practicality of the solutions obtained through static analysis may be restricted if the operational state of the multi-energy prosumer components strays considerably from a fixed static operation [10]. This approach failed to incorporate the stochasticity of meteorological conditions, peak electrical and thermal demand events, or the system's dynamic transitional behaviours.

The authors of [11–13] proposed several optimisation algorithms to solve the power dispatch problem, considering carbon footprint, optimal power flows, costs, and emissions. Furthermore, these optimisation procedures are limited by constraints within the framework and could not be adopted under extreme weather conditions, peak loads and abrupt operating changes.

In [14], a 24-h scheduling horizon was considered to minimise the system operating cost and improve the system energy-efficiency. However, the dynamic behaviour and power dispatch was not analysed. In [15], a weekly horizon was studied for a multi-energy prosumer that focused on adaptive robust optimisation under uncertain renewable power generation. Authors in [16] presented a multi-energy reinforcement learning method to tackle the energy coordination challenge associated with local trading within a highly efficient double-action market. Consistent with comparable literature, the validity of the reported benefits is confined to the proposed constraints, neglecting transient phenomena and the disparate time constants inherent to the thermal and electrical dynamics.

Two primary objective functions have been explored when addressing energy management within multi-energy systems: cost optimisation and the reduction of greenhouse gas emissions into the atmosphere. In [17], a day-ahead scheduling framework for multi-carrier microgrids, encompassing electricity, heat, and hydrogen systems, was introduced. Utilising stochastic optimisation, the model aimed to minimise both operational and environmental costs. System flexibility was enhanced through the integration of demand response programs and thermal comfort considerations. The methodology was implemented as a mixed-integer linear programming (MILP) problem. The results highlighted that the combined application of energy storage, demand response, and thermal comfort strategies led to a 12.31% reduction in microgrid costs and a 17.25% rise in profits for the distribution company.

In [18], a MILP was employed to study combined cooling, heating, and electrical microgrids. This study investigated the economic implications and energy conservation potential of heat pumps combined with energy storage devices, specifically under a time-of-use electricity pricing framework. The analysed system configuration comprised a ground source heat pump, an ESS and RETs, all optimised to achieve minimal total operating expenditures. The results indicated that heat pumps and ESS enhanced system flexibility, leading to significant economic benefits.

In [19], a multi-agent planning framework was formulated for integrated energy systems. Its primary objective was to enhance the capacity setups and energy scheduling strategies within an electricity-heat-hydrogen sharing paradigm. Utilising the alternating direction method of multipliers, the approach ensured confidentiality and equitable distribution of benefits. Seasonal simulations revealed a significant annual reduction in costs and CO_2 emissions, confirming the viability of the multi-energy system.

An optimisation scheduling model integrating carbon capture and storage (CCS) with renewable energy was presented in [20]. Simulation results, obtained via an enhanced particle swarm optimisation algorithm, indicated that the integration of CCS yielded a 74.4% reduction in carbon emissions and a 37.9% decrease in overall costs, thereby improving both low-carbon and economic efficiency.

A low-carbon economic dispatch model was developed in [21] for integrated energy systems, incorporating CCS, power-to-gas, and combined heat and power units. A carbon mathematical model was employed to limit emissions, while an optimal scheduling strategy aimed to minimise total operational costs. The model was verified through several scenarios, assessing the effects of carbon trading parameters on carbon reduction and economic efficiency.

Static analyses prevalent in the study of multi-energy systems primarily focus on optimising costs or emissions [14–21]. The MILP method is commonly adopted to solve the optimal operation problem [17,18]. The models used are typically linearised around a specific operating point [4–6] and constrained by predefined historical data or established restrictions [11–13].

The extant research reveals a significant deficiency in the modelling and control of transient behaviour for multi-energy prosumers. Consequently, adopting a non-static perspective establishes a new research horizon, targeting the integrated regulation of multiple, coupled energy carriers essential for effective real-time energy allocation. To achieve a robust control response and expand the operational envelope beyond linearised models with fixed constraints, it is crucial to account for fluctuating operational parameters. These include the charge level (SOC) of energy storage assets (ESSs), varying meteorological conditions, and the distinct temporal dynamics governing the electrical and thermal systems.

In response, this manuscript details an adaptive control framework for a grid-interfaced multi-energy prosumer. The system architecture integrates a photovoltaic (PV) power plant as the renewable source, a lithium-ion battery ESS (which mitigates renewable intermittency and offers local resiliency), and both gas and electric boilers for thermal generation. A novel state-dependent EMS was developed to ensure coordinated functioning across these energy carriers. This framework defines a trio of operational states: low temperature (LTM), normal temperature (NTM), and high temperature (HTM). The proposed EMS adaptively regulates the functional modes of the thermal sources, adjusting their operation in real- time based on available renewable energy to concurrently satisfy both electrical and thermal demands.

The primary aim of the EMS is to avoid the dependency on the utility grid, while establishing the consumption of on-site renewable generation to meet both electrical and thermal demands. The key originality of this paper lies in its approach for setting the thermal sources' operational state and controlling power flows through a battery energy storage system (BESS). This control strategy is dependent on instantaneous renewable generation and the current BESS state of charge (SOC).

The principal contributions of this manuscript are:

1. A dynamic control framework, with a 0.02 s sampling interval, for a multi-energy prosumer integrating electrical and thermal energy vectors with RETs and BESS.
2. The design of a novel, state-oriented EMS developed for the efficient management of energy distribution within the prosumer architecture.
3. Comprehensive verification of the prosumer model and EMS through a 4-h simulation under variable meteorological conditions and fluctuating demand profiles. This is complemented by a sensitivity analysis, based on 250 1-h simulations, which confirms robust control performance and reduced grid consumption across diverse irradiance, water demand, heating demand, and initial SOC scenarios.
4. Real-time experimental validation using a hardware-in-the-loop (HIL) configuration. This setup involved executing the multi-energy prosumer model on an OPAL4512 unit while the control system was deployed on a dSPACE MicroLabBox prototype. The HIL results corroborate the proposed EMS's effectiveness under realistic operational conditions.

The subsequent sections of this manuscript are structured as follows: Section 2 outlines the proposed control architecture and the EMS. Section 3 details the dynamic modelling of the multi-energy prosumer.

Section 4 discusses the results obtained from both simulations and real-time experiments. Finally, Section 5 provides the main conclusions of the study and closes the paper.

2. Control scheme and energy management system

Fig. 1 depicts the control framework proposed for the multi-energy prosumer, whose architecture is detailed in Section 3. The strategy is predicated on dynamically determining the operational set-points of the electric and gas boilers as a function of the PV power plant's generation.

The heating load operation is initiated by a pump that circulates water through the thermal bus. This central bus interconnects the system's thermal components: the gas boiler, the underfloor heating load, and the electric boiler. The EMS provides temperature references to the gas boiler, which controls the thermal bus. The electric boiler is then engaged to provide supplemental heating, ensuring the hot water demand requirements are met.

Dynamic adjustments to the water temperature are necessary during operation, prompted by variations in water flow and underfloor heating demand. This necessitates the active regulation of the electric boiler's power demand to fulfil these load requirements.

2.1. Control loops

The local management of the thermal sources and the BESS is performed by dedicated control systems. As previously mentioned, the heating process is characterised by prevalent fluctuations in hot water and underfloor heating flows. Consequently, a thermal bus control loop is tasked with maintaining the bus temperature (T_{bus}) at its specified reference value (T_{bus}^{ref}). This objective is achieved using a proportional-integral (PI) controller that governs T_{bus} by modulating the gas boiler's power output. This modulation, which heats the incoming water to meet comfort and hot water demands, ensures the delivered power aligns with thermal requirements, thereby avoiding a binary all-or-nothing control strategy.

The electric boiler's temperature control subsystem manages the output temperature (T_{EB}) according to setpoints provided by the EMS. Effective thermal regulation is achieved by implementing a hysteresis control cycle. In this process, the EMS establishes the maximum temperature (T_{EB}^{max}), and the minimum temperature for the cycle (T_{EB}^{min}) is set 4 °C lower. Consequently, the electric boiler is activated until T_{EB}^{max} is reached and deactivated until the T_{EB}^{min} threshold is crossed. This strategy ensures precise temperature control without requiring continuous power modulation. It should also be noted that the PV power plant operates using a 'perturb and observe' (P&O) algorithm to execute its maximum power point tracking (MPPT) strategy. This algorithm utilises the PV voltage and current to compute the maximum voltage point for any given operational condition.

The BESS control is performed through a dynamic SOC control loop. The BESS power is limited in both charging and discharging modes according to:

$$P_{BESS,dis}^{max} = min\left(P_{BESS}^{rated}, \frac{E_{BESS}^{rated}}{\Delta t}\cdot\left(\frac{SOC - SOC_{min}}{100}\right)\right) \quad (1)$$

$$P_{BESS,ch}^{max} = min\left(P_{BESS}^{rated}, \frac{E_{BESS}^{rated}}{\Delta t}\cdot\left(\frac{SOC_{max} - SOC}{100}\right)\right) \quad (2)$$

where $P_{BESS,dis}^{max}$ and $P_{BESS,ch}^{max}$ are the maximum BESS power in discharging and charging mode and E_{BESS}^{nom} is the rated BESS energy.

The BESS output power is restricted during discharging to prevent exceeding the rated power. Furthermore, a minimal SOC threshold is imposed to safeguard the BESS lifespan by preventing deep discharge, which can lead to premature degradation. In this paper, the minimal SOC value (SOC_{min}) was set to 20%. Similarly, the BESS power is limited to avoid overcharging. The maximum SOC value (SOC_{max}) was set to 95% to ensure optimal BESS health and life.

2.2. Energy management system

In a multi-energy prosumer, the coordinated operation between electricity and heat vectors is essential to achieve an efficient energy management. To achieve this, a state-based EMS was designed to manage the thermal sources according to the PV power plant energy production. Owing the fact that the PV plant is limited to weather conditions, the BESS supports renewable energy production. Based on these premises, the state-based EMS was conceptualised to achieve the self-sufficiency of the multi-energy prosumer. The state-based EMS computes P'_{NET} and defines five operating states according to the flowchart shown in Fig. 2.

While the proposed EMS is validated using the architecture depicted in Fig. 3, the control logic is formulated as a generalised methodology applicable to a broad spectrum of multi-energy prosumers. The framework is grounded in fundamental energy balance principles, utilising universal state variables that facilitate the seamless integration of additional energy vectors. The primary decision-making variable, the gross net power (P'_{NET}) is defined as the algebraic sum of all renewable generation and the aggregate electrical demand:

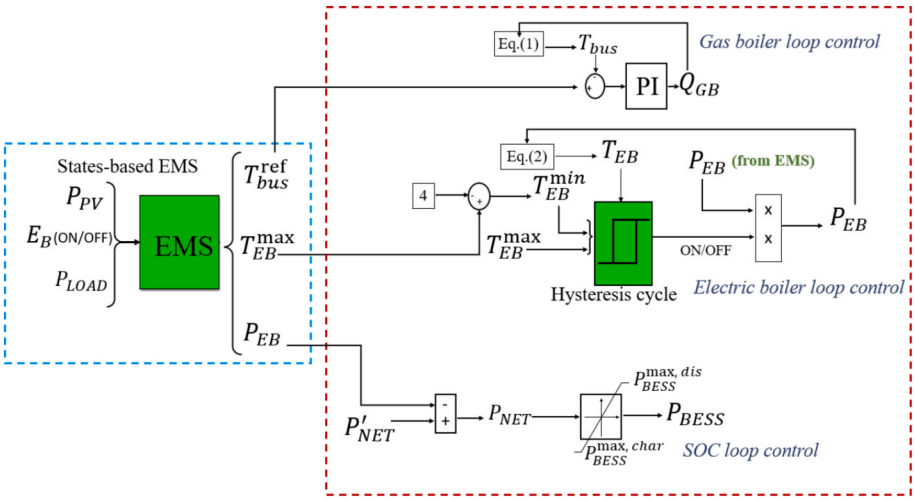

Fig. 1. Overall control scheme.

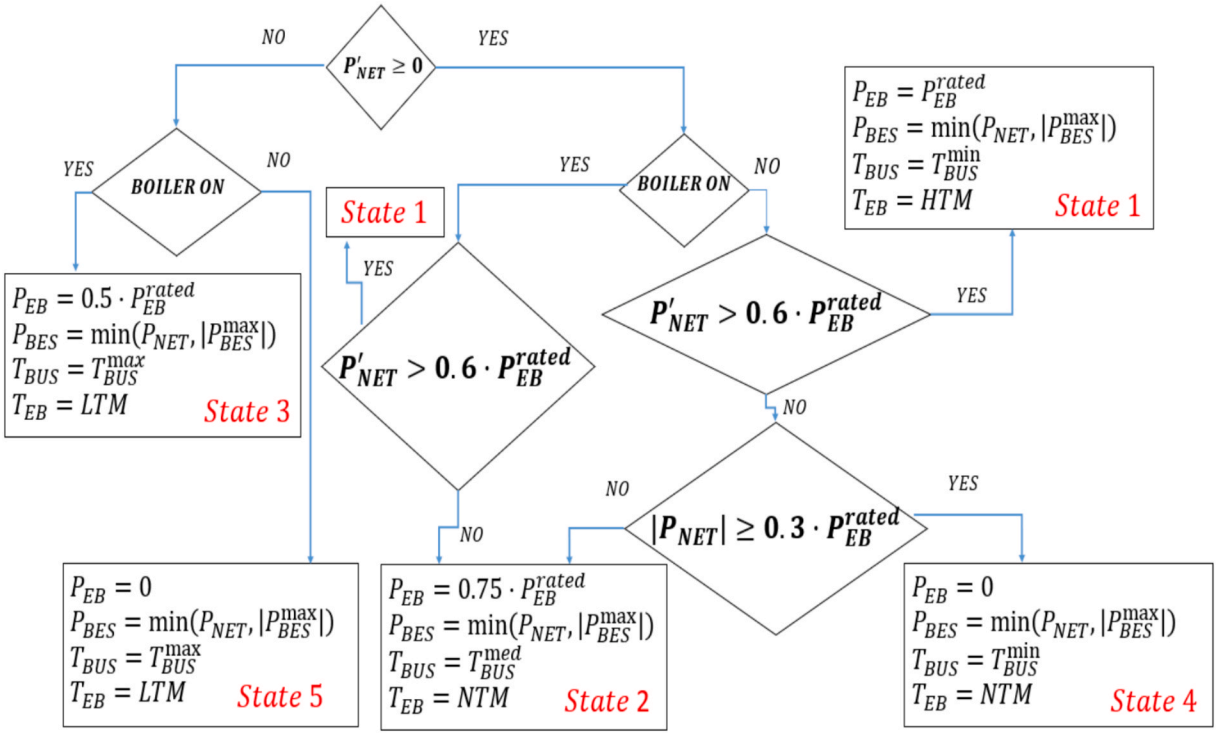

Fig. 2. State-based EMS flowchart.

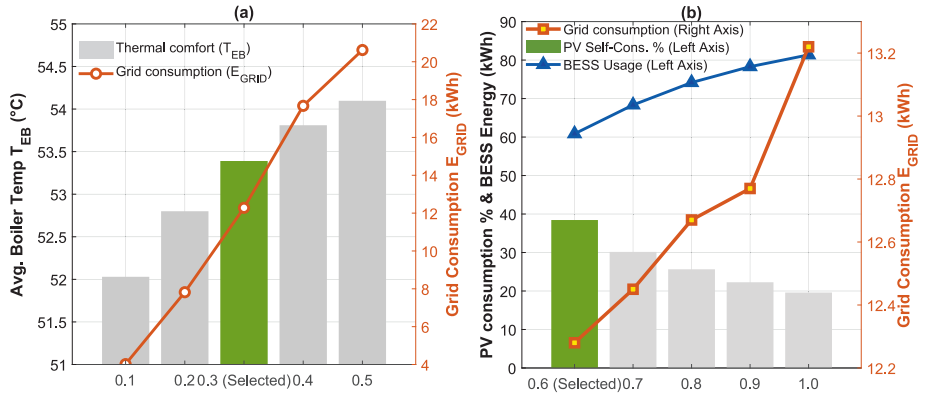

Fig. 3. State-based sensitivity analysis parameter: (a) lower activation threshold and (b) upper activation threshold.

$$P'_{NET} = \sum P_{REN} - \sum P_{LOAD} \tag{3}$$

where $\sum P_{REN}$ represents the summation of all available renewable energy sources and $\sum P_{LOAD}$ accounts for the total electrical load. In the specific case study presented in Section 3, $\sum P_{REN}$ comprises the PV production, while P_{LOAD} represents the prosumer's domestic demand. This modular approach ensures that the state-based logic—governed by the surplus or deficit of P'_{NET} remains invariant and scalable regardless of the specific prosumer configuration. Furthermore, the thermal management is decoupled from the electrical layer through generic temperature references and hysteresis-based control. This decoupling allows the EMS to be compatible with diverse thermal storage technologies and heating units (e.g., electric boilers, heat pumps, or gas heaters) without structural modifications to the control scheme. By abstracting the control logic from physical components into generic energy carriers, the proposed EMS provides a robust framework capable of managing complex, hybrid thermal-electrical systems without reconfiguration.

Positive values of P'_{NET} mean that the multi-energy prosumer manages surplus renewable energy, and the electricity vector is the principal energy carrier to supply the demand. On the other hand, negative values of P'_{NET} indicate a deficit in renewable generation relative to current demand, a condition that necessitates BESS discharge to avoid importing power from the local grid.

Once the electric load is fulfilled, the next step in the EMS is to supply the electric boiler demand according to the available energy. The net power (P_{NET}) is defined as the difference between P'_{NET} and the electric boiler power:

$$P_{NET} = P'_{NET} - P_{EB} \tag{4}$$

where P_{NET} also represents the power that the BESS must control to avoid the consumption of the local grid.

The state-based EMS is constructed around three inputs: the PV power (P_{PV}), the operating state of the electric boiler regarding the hysteresis cycle ($E_{B-ON/OFF}$) and the electric load (P_{LOAD}). It generates three outputs: the maximum temperature of the hysteresis cycle for the electric boiler (T_{EB}^{max}), the reference temperature for the thermal bus

(T_{bus}) and the electric boiler reference power (P_{EB}).

HTM: The high-temperature state is initiated when the multi-energy prosumer's renewable generation exceeds the residential electricity demand ($P'_{NET} > 0$) and the gas boiler's consumption. This state is specifically triggered if the electric boiler is active and the renewable surplus P'_{NET} surpasses 60% of the electric boiler's rated capacity (P_{EB}^{rated}). This 60% threshold ensures the energy is supplied by the PV plant, not the BESS, preventing the BESS from discharging below SOC_{min}. If these conditions are met while the boiler is inactive, the EMS commands its activation. In this mode, the electricity vector is the primary energy carrier, and the electric boiler operates at rated power. Consequently, gas consumption is reduced, with the gas boiler operating at a low-temperature setpoint (30 °C). The BESS manages the electrical energy balance, charging or discharging according to its SOC. The electric boiler is controlled within a 56–60 °C range.

NTM: The normal temperature state (NTM) is engaged when renewable energy availability is lower than in the HTM, specifically when $P'_{NET} < 0.6 \cdot P_{EB}^{rated}$ and $P'_{NET} > 0$, $P_{EB} > 0$. In this operational mode, the electric boiler's power is derated to $0.75 \cdot P_{EB}^{rated}$, while the gas boiler's temperature is elevated to increase its contribution to the hot water circuit. This strategy enhances operational efficiency by reducing the thermal increment required from the electric boiler. This situation arises because activating the electric boiler does not necessarily result in a significant surplus of energy. The control setpoints for this mode are 52–56 °C for the electric boiler and 32.5 °C for the gas boiler.

LTM: The low-temperature state is triggered when the multi-energy prosumer's renewable generation is insufficient to cover residential electricity demand ($P'_{NET} < 0$). This deficit necessitates BESS discharge to prevent reliance on the electrical grid. In this state, the gas boiler operates at its maximum temperature (35 °C), serving as the principal energy carrier for the thermal loads. If the hysteresis cycle requires the electric boiler's activation, it is engaged at a low-temperature setpoint (48–52 °C) and a power level of $0.5 \cdot P_{EB}^{rated}$.

Off Mode (NTM): When the amount of renewable energy available is greater than in LTM, the electric boiler is controlled in an inactive mode within the temperature range of NTM. This state occurs when $P'_{NET} > 0$, $P_{EB} < 0$, $P'_{NET} < 0.6 \cdot P_{EB}^{rated}$ and $|P_{NET}| > 0.3 \cdot P_{EB}^{rated}$. This scenario is selected since there is a high amount of energy needed to supply the electric boiler, and the BESS would not have enough capacity to meet the demand.

Off Mode (LTM): In the scenario where the available renewable energy is highly insufficient to meet demand and the gas boiler is turned off, it should remain off to prevent further increasing the electrical consumption of the multi-energy prosumer. This state occurs when $P'_{NET} < 0$ and $P_{EB} < 0$. The thermal bus is controlled at maximum temperature (35 °C) due to the lack of renewable energy.

Table 1 collects the main control scheme parameters:

The configuration of the proposed EMS is governed by a rule-based expert approach aimed at ensuring operational stability and asset preservation. Consequently, the selection of the control parameters—specifically the boiler power levels (0.5, 0.75, and 1.0 times P_{EB}^{rated}) and the renewable surplus margins (high and low) represent a robust design compromise between thermal energy harvesting and electrical system reliability. Regarding the electric boiler, the discretised power levels reflect the operational nature of modern multi-stage thermal actuators. This approach avoids the limitations of a conventional binary (ON/OFF) control, thereby mitigating high-frequency power fluctuations and control 'chattering' that could endanger the integrity of the power electronics during real-time operation. Specifically, these power stages are realised by varying the number of active heating elements (resistances) within the electric boiler, enabling the system to modulate the thermal load according to the instantaneous availability of energy surplus.

Table 1
Control scheme parameters.

Variable	Value
Minimum SOC, SOC_{min}	20
Maximum SOC, SOC_{max}	95
High temperature mode, HTM	$P_{EB} = P_{EB}^{rated}$ $T_{bus} = 30\ ^{\circ}C$ $T_{EB}^{max} = 56-60\ ^{\circ}C$
Normal temperature mode, NTM	$P_{EB} = 0.75 \cdot P_{EB}^{rated} T_{bus} = 32.5\ ^{\circ}C$ $T_{EB}^{max} = 52-56\ ^{\circ}C$
Low temperature mode, LTM	$P_{EB} = 0.5 \cdot P_{EB}^{rated} T_{bus} = 35\ ^{\circ}C$ $T_{EB}^{max} = 48-52\ ^{\circ}C$

To rigorously substantiate the selection of the surplus thresholds and verify their effectiveness beyond theoretical assumptions, a comprehensive quantitative sensitivity analysis was conducted, the results of which are illustrated in Fig. 3. This analysis was designed to evaluate the system's performance across a full operational spectrum, subjecting the EMS to highly dynamic boundary conditions characterised by PV generation varying from 0 to 18 kW, electrical demand ranging from 0 to 13 kW, and thermal heating demand fluctuating between 1 and 3.5 kW. By systematically mapping the control landscape, the analysis reveals that the selected values of 0.3 and 0.6 are not arbitrary, but rather represent distinct points of inflection where system efficiency is maximised before diminishing returns or operational penalties begin to dominate.

The first parametric sweep, presented in Fig. 3a, examines the lower threshold, by varying values from 0.1 to 0.5 to determine the minimum surplus required to sustain boiler operation. The empirical data identifies 0.3 as the critical effective limit. At this selected threshold, the system successfully maintains a high degree of thermal comfort, achieving an average boiler temperature (T_{EB}) of 53.39 °C, while keeping grid consumption contained at 12.28 kWh. The analysis demonstrates that tightening this constraint further, such as increasing the threshold to 0.4, yields a negligible thermodynamic benefit, raising T_{EB} marginally to 53.81 °C. However, this slight gain incurs a severe energy penalty, as it forces the system to import significantly more electricity (17.67 kWh) to maintain the temperature. Thus, 0.3 is validated as the optimal trade-off point where comfort is secured without triggering the non-linear rise in grid dependency observed at higher values. This inefficiency is exacerbated when extending the threshold to the upper bound of 0.5, where grid consumption escalates disproportionately to 20.62 kWh, confirming a regime of diminishing returns. Conversely, relaxing the threshold to the lower bounds of 0.1 and 0.2 significantly reduces grid reliance (dropping to 4.02 kWh and 7.82 kWh, respectively). Yet, this conservation strategy proves overly conservative regarding thermal accumulation; it results in lower average temperatures (52.03 °C and 52.80 °C), which indicates an under-utilisation of the boiler's capacity and risks compromising comfort during subsequent demand peaks.

The second analysis, shown in Fig. 3b, investigates the upper activation threshold by sweeping from 0.6 to 1.0 to assess the impact on renewable harvesting efficiency. The results unequivocally demonstrate that 0.6 is the most effective threshold for maximising self-sufficiency, achieving a direct PV utilisation rate of 38.48% and limiting the BESS energy throughput to 60.85 kWh. Conversely, setting the threshold to the maximum value of 1.0 reduces prosumer efficiency. By requiring a 100% surplus before activating the boiler, the system fails to capture available solar energy, causing direct PV utilisation to drop to 19.60%. To compensate for this missed energy, the BESS must supply the deficit, which drives its energy throughput up to 81.35 kWh to satisfy the same thermal demand. This indicates that higher threshold values effectively delay boiler activation, causing the system to miss valuable windows of solar surplus and unnecessarily accelerating BESS degradation through increased cycling.

Consequently, the chosen thresholds of 0.6 and 0.3 are confirmed by empirical evidence as the appropriate setpoints to function as hierarchical decision gates for energy sourcing. By requiring a significant PV

surplus before initiating or increasing the boiler's power, the EMS prevents the BESS from being forced to compensate for high-power transients. This is critical to avoid driving the BESS SOC toward its lower safety limit for secondary thermal objectives. This logic prioritises the BESS for critical residential electrical loads, treating the thermal vector as a non-critical flexible demand. The functional adequacy of these setpoints was further confirmed through the HIL experimental verification described in Section 4, where the system demonstrated a stable and grid-independent response across the tested scenarios.

3. Dynamic modelling of multi-energy prosumer

The case study considered in this research represents a typical multi-energy prosumer configuration, integrating the primary thermal and electrical generation sources found in contemporary residential and light-commercial environments. In such setups, thermal provision predominantly comprises gas and electric boilers, whereas residential renewable generation is typically based on PV plants due to their cost-effectiveness and seamless integration. Furthermore, BESS are commonly incorporated to mitigate and smooth the inherent stochastic fluctuations of renewable output.

Numerous studies in the literature have adopted similar architectures to investigate multi-energy prosumer dynamics. For instance, the integration of natural gas-fired boilers and PV panels was explored in [22] to optimise the utilisation of waste heat and minimise the carbon footprint of nearly-zero exergy district prosumers. In [23], a combination of both gas and electric boilers was utilised alongside PV and BESS to evaluate optimal bidding strategies within double-auction electricity-heat markets. Comparative analyses have also assessed various thermal configurations, including the use of natural gas-fired boilers in conjunction with PV installations for single-family houses [24].

Similarly, a configuration involving a gas boiler, PV panels, and BESS was examined in [25] to facilitate price-based demand response schemes designed to motivate prosumers to adjust their distributed energy resource operations. Moreover, the combined use of PV panels and electric boilers has been considered in [26] to conduct risk assessments of integrated electrical, natural gas, and district heating systems. Consequently, by incorporating these established and representative elements, this study provides a robust and realistic foundation for conducting a novel analysis of dynamic, real-time control frameworks for multi-energy prosumers.

The architecture of the multi-energy prosumer is depicted in Fig. 4. This system integrates both thermal and electrical components. Within the thermal subsystem, a gas boiler is utilised to regulate the temperature of the hot water circuit, while a 23-kW electric boiler provides supplemental capacity to satisfy the hot water demand. Furthermore, an underfloor heating load, representing the residential heating demand, is coupled to this hot water circuit.

The electrical side of the multi-energy prosumer encompasses a three-phase 400 V bus, in which the following components are connected: a PV generator with a peak capacity of 18 kW. The layout of the PV power plant comprises six parallel strings, each with 10 modules connected in series. Each string has a maximum power extraction capability of 300 W. A Lithium-Ion BESS, with a 26.6 kWh rated capacity, is integrated to buffer energy production and mitigate the variability stemming from fluctuating energy demand and intermittent PV power generation. A variable electrical load, designed to simulate residential consumption, is coupled to the 400 V bus. Furthermore, the multi-energy prosumer is interfaced with the three-phase utility grid, which serves as an ancillary power source.

It is essential to specify that the actively controlled (i.e., dispatchable) components within the multi-energy prosumer are the gas and electric boilers, in conjunction with the BESS. Conversely, the PV power plant is non-dispatchable, operating under a maximum power point tracking (MPPT) algorithm to maximise its generation. The local grid functions as the balancing authority, absorbing any surplus electrical energy or supplying any deficit required to meet demand fluctuations. The main model parameters are summarised in Table 2.

3.1. Model of thermal system

The present study incorporates a hybrid thermal source consisting of both an electric boiler and a gas boiler as the core generation units. The overarching operational objective is to prioritise prosumer self-sufficiency by avoiding the energy consumption from the primary grid. In scenarios where instantaneous renewable generation or the available capacity within the BESS proves insufficient to sustain the electric boiler's requirements, the system must nonetheless guarantee that the thermal load is fully satisfied.

Table 2
Model parameters.

Variable	Value
Three phase voltage level	400 V
PV power plated capacity	18 kW
PV modules	60 – six strings of 10 series connection
PV open-circuit voltage (V_{oc})	46.12 V
PV short-circuit current (I_{sc})	8.56 A
BESS rated power	26.2 kW
BESS capacity	76 Ah
Electric boiler rated power	23 kW
Electric boiler capacity	300 L

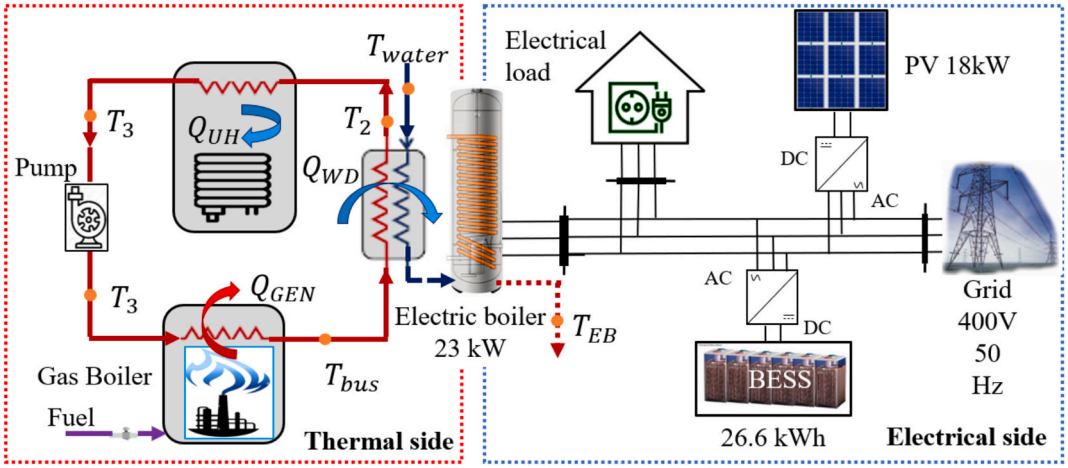

Fig. 4. Schematic configuration of the proposed multi-energy prosumer.

Consequently, the gas boiler is integrated as a secondary thermal source to complement the electric boiler's operation. Within this framework, the gas boiler serves as a critical backup unit that ensures thermal supply security during periods of significantly attenuated electrical availability, thereby maintaining the balance between decarbonisation and reliability. To this end, the electric boiler is dedicated to meeting domestic hot water demand, whereas the gas boiler handles the heating requirements. This hybrid approach, which prioritises the electrical vector for thermal generation while maintaining a high-availability gas backup, aligns with several established studies in the literature. Similar configurations have been explored in [27–29], where the combination of electric and gas boiler was adopted.

The MATLAB Simulink CARNOT toolbox extension was adopted to dynamically model the thermal elements within the multi-energy prosumer shown in Fig. 4. Tailored for high-voltage AC systems, this toolbox was developed by the Institute of Solar Research in Juelich, Germany [30]. It incorporates thermodynamic and energy engineering models [31]. The standard components of a thermal system are available in the library as blocksets, each corresponding to conventional elements, such as pumps or heat exchangers.

CARNOT Toolbox models have been extensively recognised and utilised within the scientific literature for the high-fidelity dynamic accuracy of complex thermal components. The reliability of this framework in representing transient thermal behaviour is substantiated by its successful application in various validated scenarios. Specifically, the toolbox was employed in [32] to simulate residential district heating grids, where the specific gas boiler block was utilised to accurately replicate building heat demand and energy-saving potentials. This study confirms the capability of the CARNOT environment to model individual building dynamics and boiler operations within large-scale urban energy clusters. Furthermore, the suitability of the CARNOT library for high-precision, real-time applications is evidenced in [33], where a detailed dynamic model was developed to emulate a fossil-fired steam boiler system. This particular model was rigorously verified through HIL testing, confirming that the toolbox provides the necessary numerical stability and physical accuracy to represent complex thermal transients in real-time frameworks. In a similar vein, the validated modelling of fundamental plant components thermal storage tanks was demonstrated in [34]. This research reinforces the toolbox's capacity to maintain high physical fidelity across diverse multi-generation architectures under fluctuating climatic conditions.

Moreover, the versatility of the framework for residential and institutional applications is further supported by the work in [35], where a multi-room simulation model of an educational building was constructed using the CARNOT Toolbox. This implementation was specifically designed to capture the intricate thermal dynamics and heat storage capacities of the building envelope and its associated heating circuits, including electric boilers. Consequently, the integration of these models—independently validated across both boiler units and residential architectures—ensures that the dynamic thermal simulation environment established in this study provides a robust, reliable, and highly accurate framework.

The available model for the gas boiler simplifies its representation, primarily focusing on the heat input into the combustion chamber. It neglects any constraints originating from the process or combustion control, such as the initial burner control during start-up. To address the water circuit of the boiler, a multi-node model is employed to account for time-dependent conditions. The governing differential equation for the gas boiler is outlined in [31] and is given as:

$$\left(m \cdot c \cdot \frac{1}{N}\right) \cdot \frac{dT_{bus}}{dt} = \left(U \cdot A \cdot \frac{1}{N}\right) \cdot (T_{amb} - T_{bus}) + (\dot{m}_{bus} \cdot c_f) \cdot (T_{in} - T_{bus}) + Q_{GB} \tag{5}$$

where m denotes the mass of the boiler, c the heat capacity boiler, N the number of nodes, $U{\cdot}A$ the heat loss coefficient to ambient, T_{amb} the ambient temperature, T_{bus} the bus temperature, $\dot{m}_{bus}$ the mass flow rate in the thermal bus, c_f the heat capacity of fluid, T_{in} the input temperature in the boiler and Q_{GB} the heat injected by the gas boiler.

The electric boiler is modelled as an electric heater that converts electrical power into thermal energy to raise the temperature of the incoming water mass flow, thereby satisfying domestic hot water requirements. A thermal node architecture is employed to represent the heater's thermal inertia, which also accounts for heat losses to the ambient environment. The electric boiler's model is defined as follows [36]:

$$C_{EB} \cdot \frac{dT_{EB}}{dt} = U \cdot A \cdot (T_{amb} - T_{EB}) + (\dot{m}_W \cdot c_p) \cdot (T_{bus} - T_{EB}) + P_{EB} \tag{6}$$

where C_{EB} represents the electric boiler's thermal capacity, T_{EB} is the electric boiler output temperature, and $\dot{m}_W$ corresponds to the mass flow rate in the electric boiler. Furthermore, c_p signifies the fluid's heat capacity (at constant pressure), and P_{EB} is the power consumed by the gas boiler.

3.2. Modelling of electrical vector

The PV system configuration described in [37] was here adopted due to its well-established accuracy and simplicity [38]. The PV system is represented using the five-parameter single-diode model within the MATLAB/Simulink SimPowerSystems environment. This model accounts for the non-linear relationship between current and voltage by incorporating a regulated current source, a diode, and both series (R_s) and parallel (R_{sh}) resistances. To guarantee the accuracy of the electrical generation profile, the model was parameterised using the technical specifications of a real-world American Solar Wholesale ASW-300 M module. The simulated PV array was calibrated to match the manufacturer's datasheet at standard test conditions (STC), featuring a maximum power (P_{max}) of 300.05 W, an open-circuit voltage (V_{oc}) of 46.12 V, and a short-circuit current (I_{sc}) of 8.56 A. This high-fidelity parameterisation ensures that the simulation accurately replicates the transient power output of the physical PV plant under fluctuating irradiance and temperature levels. The mathematical formulation of the PV power plant is as follows:

$$I_{PV} = I_L - I_{sat}\left(e^{\frac{q(V_{PV}+I_{PV}R_s)}{N_s K T_{PV}}}\right) - (V_{PV} + I_{PV}R_S)/R_{sh} \tag{7}$$

where I_{PV} represents the PV output current, I_L is the light-generated current, I_{sat} denotes the saturation current, and N_s is the number of series-connected modules. Additionally, q is the electron charge, V_{PV} is the output PV voltage, R_s is the series resistance, K is the Boltzmann constant, T_{PV} is the PV cell temperature, and R_{sh} is the shunt resistance.

The BESS has been modelled using the validated Lithium-Ion framework from the SimPowerSystems toolbox [39]. It has been detailed the specific discharge parameters (e.g., internal resistance, nominal voltage, and capacity) to ensure the model captures the non-linear dynamics of the storage unit with high fidelity. The BESS model is formulated to capture its dynamic response and characteristic voltage-current (V-I) and voltage-SOC (V-SOC) curves. This is achieved using an equivalent circuit, comprising a series resistance and a variable voltage source, which ensures a high-fidelity representation of the BESS's behaviour. Furthermore, the SOC is chosen as a critical parameter requiring robust control mechanisms to prevent operations beyond the designated overcharging or excessive discharging thresholds. The SOC is determined by monitoring the BESS current (I_{BESS}) relative to the initial SOC (SOC_O) and the BESS rated capacity (Q_{BESS}).

$$SOC(\%) = SOC_O(\%) - 100\left(\frac{\int I_{BESS} \cdot dt}{Q_{BESS}}\right) \tag{8}$$

4. Results and discussion

The objective of this section is to validate the performance of the control scheme and state-based EMS of Section 2 for the dynamic multi-energy prosumer model defined in Section 3. For this purpose, four different case studies are carried out: (4.1) multi-energy prosumer performance in a 4-h scenario subjected to different atmospheric conditions, varying electrical and thermal loads; (4.2) sensitivity analysis to verify the control scheme under extreme operating conditions and to evidence the minimum reliance in the primary grid to feed the loads; (4.3) real-time validation through HIL experimentation with real control and measurement equipment and (4.4) long-time comparison against fuzzy logic (FL) control scheme.

4.1. General multi-energy prosumer performance

The multi-energy prosumer's general performance was evaluated using a 4-h simulation conducted in MATLAB/Simulink. The objective of this analysis is to assess the control scheme's effectiveness and the proposed state-based EMS's response under several operational scenarios. A sampling time of 0.02 s was selected to achieve an adequate transient response for both thermal and electrical components, accounting for their different dynamic time constants. The input variables for the prosumer are detailed in Fig. 5, showing the irradiance profile (Fig. 5a), the hot water demand mass flow (m_W) (Fig. 4b), and the underfloor heating demand (Q_{UH}) (Fig. 5c). The initial state of charge for the BESS was set at 90%.

The electrical energy balance is illustrated in Fig. 6a. Positive values denote that energy is delivered to the multi-energy prosumer, while negative values represent energy consumed by the multi-energy prosumer. From 0 to 2500 s into the simulation, The PV power plant delivers 16.2 kW and the electrical load requires 1 kW. In this situation, there is sufficient renewable power to operate the HTM. The electric boiler is activated at 23 kW and the BESS supplies 7.8 kW to compensate the energy balance and achieve a zero consumption of the local grid.

At 2500 s into the simulation, the irradiance drops to 765 W/m^2, and the PV power plant production decreases to 13.8 kW. In this new scenario, P'_{NET} takes a value of 12.8 kW, which is lower than $0.6{\cdot}28\,kW$ ($0.6{\cdot}P_{EB}^{rated}$). Therefore, the multi-energy prosumer changes the operating mode to NTM and the electric boiler consumes 0.75 P_{EB}^{rated}.

The BESS is responsible for fulfilling the peak electric load and is charged when the electric boiler is turned off, for instance from 4900 s to 5250 s. This operating mode is maintained from 2500 s to 9000 s.

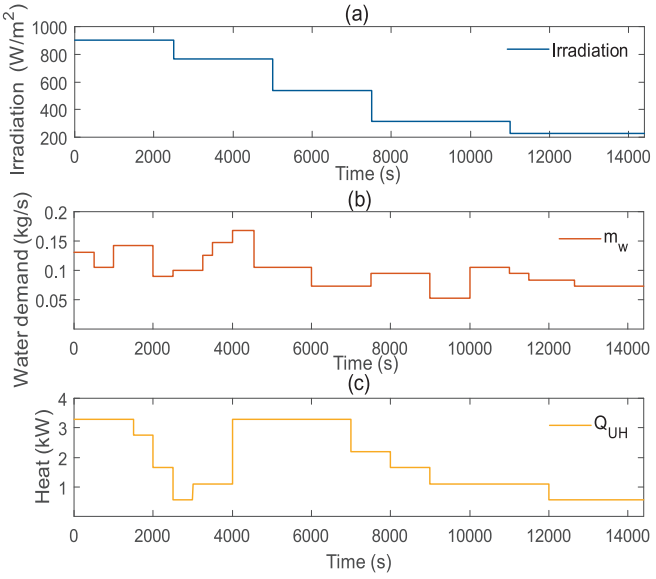

Fig. 5. Multi-energy prosumer operating parameters.

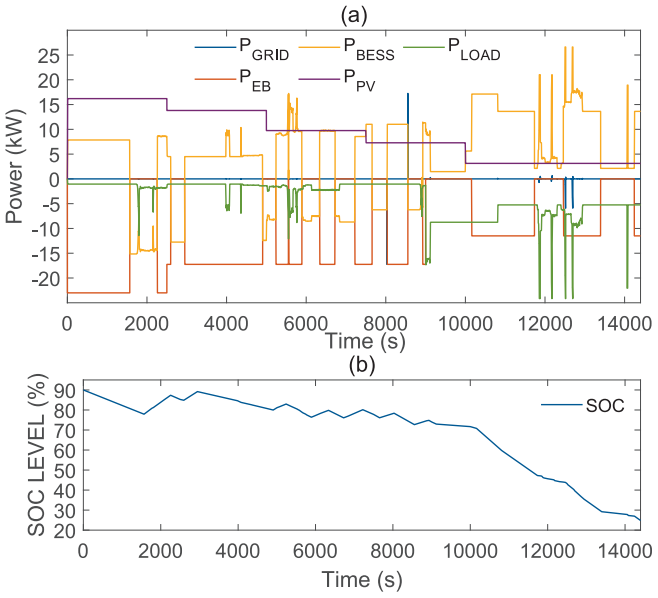

Fig. 6. (a) Electric power balance for the multi-energy prosumer, and (b) SOC of the BESS.

At 9000 s, P_{LOAD} raises to −8.3 kW and P_{PV} delivers 7.3 kW. Therefore, P'_{NET} is negative (−1 kW), denoting the low electricity available to supply the multi-energy prosumer, and the operating mode is changed from NTM to LTM. The electric boiler power now takes a value of $0.5{\cdot}P_{EB}^{rated}$ and the BESS is the main source to fulfil the demand.

It is noteworthy that from 12,000 s to 12,700 s, P_{LOAD} takes unseasonable values and the BESS is able to recognise and address properly this situation without needing the primary grid contribution. On the other hand, the SOC behaviour exhibited by the BESS is shown in Fig. 6b. The BESS is mainly discharged when the electric boiler is turned on and charged when it is turned off.

The heating balance is depicted in Fig. 7a. This represents the thermal energy injected by the gas boiler (Q_{GEN}) and the energy consumed by the hot water demand added to the underfloor heating demand (Q_{CON}). The gas boiler is responsible to keep the temperature of the thermal bus, and therefore, Q_{GEN} must be equal to Q_{CON} to achieve an adequate thermal bus control. Additionally, Fig. 7b shows the thermal energy supplied by the electric boiler to attain the hot water demand (Q_{EB}) and the heat extracted from the thermal bus owing to hot water

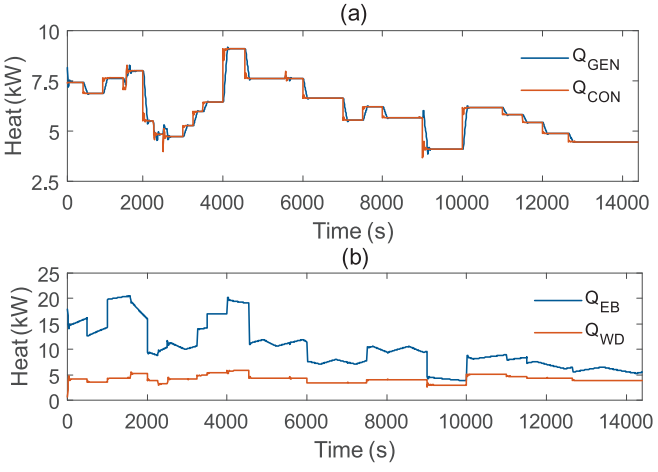

Fig. 7. (a) Heating balance for the multi-energy prosumer, and (b) electric boiler heating and hot water heating consumption.

consumption (Q_{WD}).

The temperature control of the gas and electric boiler is shown in Fig. 8a. From 0 to 2500 s into the simulation, the multi-energy prosumer operates in HTM. The electric boiler initial temperature was fixed to 52 °C. The hysteresis cycle is regulated between 60 °C as T_{EB}^{max} and 56 °C as T_{EB}^{min}. On the other hand, the thermal bus is regulated at minimum temperature, which was set at 30 °C. At 2500 s, the multi-energy prosumer changes to NTM and the hysteresis cycle manages the temperature between 55 °C and 52 °C and the gas boiler increment the temperature of the thermal bus to 32.5 °C. The temperature is increased because there is less renewable energy available in NTM. Therefore, the temperature rise that must be achieved by the electric boiler is lower if the thermal bus temperature increases. In this way, the electricity and heat vectors are interconnected, and efficient synchronisation is achieved, ensuring that demand is met.

Finally, at 9000 s into the simulation, the multi-energy prosumer operates in LTM until the end of the simulation. Owing to the lack of renewable energy in this scenario, the gas boiler increments the temperature of the thermal bus to 35 °C and the hysteresis cycle decreases the temperature reference of the electric boiler between 52 °C and 48 °C.

It can be seen that throughout the simulation a good temperature control for the three operating modes was achieved despite variations in hot water demand and underfloor heating load.

It should be highlighted that heat exchangers between thermal sources and loads are not considered ideal in this paper. Therefore, owing to the heat flow through the thermal system, there are temperature drops in the hot water circuit that must be considered to ensure a realistic representation of the heating process. The temperature drops are calculated as:

$$T_2 = \frac{\dot{m}_W \cdot T_{water} + \dot{m}_{bus} \cdot T_{bus}}{\dot{m}_{bus} \cdot c_p} \tag{9}$$

$$T_3 = T_2 - \frac{Q_{UH}}{\dot{m}_{bus} \cdot c_p} \tag{10}$$

where T_{water} is the water temperature in the local water network.

Fig. 8b denotes the temperature drops in the hot water hydraulic circuit, where it is demonstrated that the bus temperature is higher than the temperature after the hot water exchange (T_2) and similarly, T_2 is higher than the temperature after the underfloor heating exchange (T_3).

Finally, the distribution of the generated energy between the PV power plant and the BESS to meet the demand is analysed. As discussed earlier, the contribution from the electrical grid has been avoided. First, the energy generated by the PV power plant, denoted as E_{PV}, is calculated as the integral of P_{PV} over time. Similarly, the residential electricity demand, E_{LOAD}, is obtained as the integral of P_{LOAD} over time, and the demand for the electric boiler, E_{BOILER}, as the integral of P_{BOILER} over time. Results are presented in Table 3, which shows that the PV power plant has covered 84.35% of the residential demand, while the remaining 15.65% is supplied by the BESS. Regarding the electric boiler demand coverage, the PV power plant has supplied 41.02%, while the BESS has addressed 58.98% of the demand. This was expected given that the primary use of the PV plant is to supply the residential demand. The total consumption balance (obtained as the sum of E_{BOILER} and E_{LOAD}) indicates that more than half of the demand is met by the PV plant. Specifically, 52.32% is supplied by the PV plant and the remaining 47.76% by the BESS.

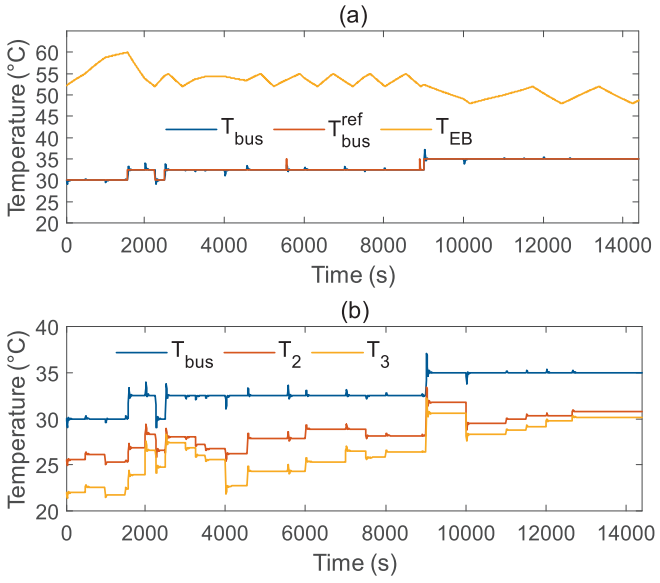

Fig. 8. (a) Temperature control for the multi-energy prosumer, and (b) nodes temperature.

4.2. Sensitivity analysis

To strengthen the findings of the proposed control scheme and state-based EMS, a comprehensive sensitivity analysis is presented in this section. This sensitivity analysis involves 250 simulations with a 1-h duration. The aim of this analysis is to examine the system ability to avoid the use of the local grid while maintaining effective thermal bus and thermal balance control.

Table 4 lists the input variables used in the sensitivity analysis and their respective ranges. Four key input variables, namely PV power plant irradiance (I), m_W, Q_{UH} and BESS initial SOC, are subjected to random variations. The BESS initial SOC is varied between 40% and 90%, I between 400 W/m^2 and 1000 W/m^2, m_W between 0.04 kg/s and 0.15 kg/s, and finally Q_{UH} between 500 W and 3500 W. Three key outputs are utilised to verify the results: the energy consumed by the local grid (E_{GRID}), calculated as the integral with respect to time of the power delivered by the grid, and the mean relative error (MRE) calculated as the average error between the measured signal and the reference value. The MRE is calculated for the bus temperature control (MRE_T) and for the thermal balance (MRE_Q).

Results from the sensitivity analysis are shown in Fig. 9, where E_{GRID} versus SOC is illustrated in Fig. 9a, E_{GRID} versus I in Fig. 9b, E_{GRID} versus m_W in Fig. 9c, and E_{GRID} versus Q_{UH} in Fig. 9d. Similarly, Figs. 9e–h and i-l shows MRE_T and MRE_Q. Table 5 summarises the mean values, standard deviation (SD) and statistical mode for E_{GRID}, MRE_T and MRE_Q across the 250 case studies examined.

The results reveal minimal local grid energy consumption, with an average consumption of $4.554{\cdot}10^{-6}$ kWh and a SD of $5.736{\cdot}10^{-5}$ kWh. On the other hand, an effective control response is ensured for the thermal bus, with an average MRE of $8.375{\cdot}10^{-6}$ °C and a SD of $3.31{\cdot}10^{-6}$ °C. The thermal balance is also verified with an average MRE of $5.12{\cdot}10^{-4}$ (W) and a standard deviation of $4.579{\cdot}10^{-5}$. The statistical results demonstrate a minimal grid participation in meeting the demand and a high accuracy in the temperature control and heating balance—confirming the effectiveness of the control system under several operating conditions.

The findings from the sensitivity analysis demonstrate the effectiveness of the dynamic control scheme under diverse and challenging

Table 3
Electricity energy dispatch.

Variable	Energy demanded (kWh)	E_{PV} (kWh)	E_{BESS} (kWh)
Residential load, E_{LOAD}	14.06	11.86 (84.35%)	2.24 (15.65%)
Electric boiler, E_{BOILER}	39.83	16.33 (41%)	23.5 (59%)
Total demand, E_{BOILER}	53.89	28.19 (52.32%)	25.74 (47.76%)

Table 4
Sensitivity analysis range.

Variable	Parameter	Range
BESS initial SOC (%)	SOC_o	[40,90]
Irradiance (W/m^2)	I	[400,1000]
Water demand (kg/s)	m_W	[0.04,0.15]
Heating demand (W)	Q_{UH}	[500,3500]

operating conditions and the adequate response of the proposed EMS to handle several scenarios and achieve the desired goals.

To demonstrate the benefits of the proposed real-time control scheme, a comparative analysis of key approaches available in the literature is presented below.

In [40], an integrated energy system was introduced within a linear coordinated energy management framework. The proposed problem was formulated as a scenario-based stochastic model using a Monte Carlo simulation, targeting optimal economic performance for energy hubs. This approach considered deviations in network temperature control. The results revealed a temperature deviation of 0.111 pu, exceeding the established limit of 0.1 pu. The real-time control results from the sensitivity analysis of the proposed EMS in this paper, based on 250 simulations, demonstrated superior temperature control performance, with an average RME of $8.375{\cdot}10^{-6}$ and a standard deviation in RME of $3.31{\cdot}10^{-5}$.

Similarly, a model predictive control (MPC) technique was implemented in [41] for the optimal multi-energy prosumer operation to enhance flexibility. However, with a time step of 15 min, the proposed MPC scheme experienced temperature control variations of up to 5% compared to the setpoint and achieved only a 1.23% reduction in main grid consumption. Nevertheless, the results obtained with the EMS presented in Section 2 of this paper exhibited a mean RME of $8.375{\cdot}10^{-6}$ across 250 different simulations and an average consumption of $4.554{\cdot}10^{-6}$ kWh.

In [42], a multi-energy prosumer for a community district was presented. A deep reinforcement learning approach (DRL) was proposed to reduce energy costs and minimise constraint violations. Regarding computational effort, the DRL required a complex control structure, resulting in convergence times of 4.53 h for the soft actor critic DRL and 5.37 h for the proposed safe-soft actor critic DRL. This level of complexity makes real-time control validation challenging for DRL approaches. Instead, the presented state-based control system allows for verification with real control equipment through an HIL platform, as demonstrated in Section 4.3, highlighting its suitability in terms of computational time and practical reproducibility.

Two EMS approaches were presented in [43]: one focused on peak shaving and another on network costs. The presented flowchart approach demonstrated a 10.38% reduction in network consumption for the peak shaving EMS and a 33.58% reduction for the EMS considering network costs. In contrast to these approaches, which achieved network consumption reduction based on the chosen strategy, this paper has shown in Section 4 that the electrical grid participation in meeting demand is minimal, with an average consumption of $4.554{\cdot}10^{-6}$ kWh under varying irradiance, SOC, and thermal demand conditions.

A similar approach was presented in [44], integrating a rolling optimisation stage with an MPC framework for residential and industrial consumers. Simulation results demonstrated that total costs and purchased electricity can be effectively reduced by participating in emergency demand response programs. These results indicated a reduction of 23.51–41.83% in electricity purchased from the grid, with a 10-minute timeframe for achieving nearly real-time demand responses. The proposed real-time SB-EMS uses a timescale of 0.02 s to accurately represent the dynamic behaviour of the multi-energy prosumer, thereby avoiding the need to procure electricity from the grid.

Similarly, three-time scales were presented in [45] based on an optimisation operation model, encompassing day-ahead scheduling, intra-day rolling, and real-time adjustment to increase renewable energy penetration. The real-time EMS used a 5-minute time scale. In this work, the timescale of 0.02 represents a more realistic approach, leading to the economic benefits previously discussed.

Table 5
Sensitivity analysis numerical results.

Variable	E_{GRID} (kWh)	MRE_T (°C)	MRE_Q (W)
$\bar{x}$ (Mean)	$4.554{\cdot}10^{-6}$	$-8.375{\cdot}10^{-6}$	$5.12{\cdot}10^{-4}$
σ (SD)	$5.736{\cdot}10^{-5}$	$-3.31{\cdot}10^{-5}$	$4.579{\cdot}10^{-5}$
Mode	$-7.646{\cdot}10^{-5}$	$-2.785{\cdot}10^{-5}$	$5.085{\cdot}10^{-4}$

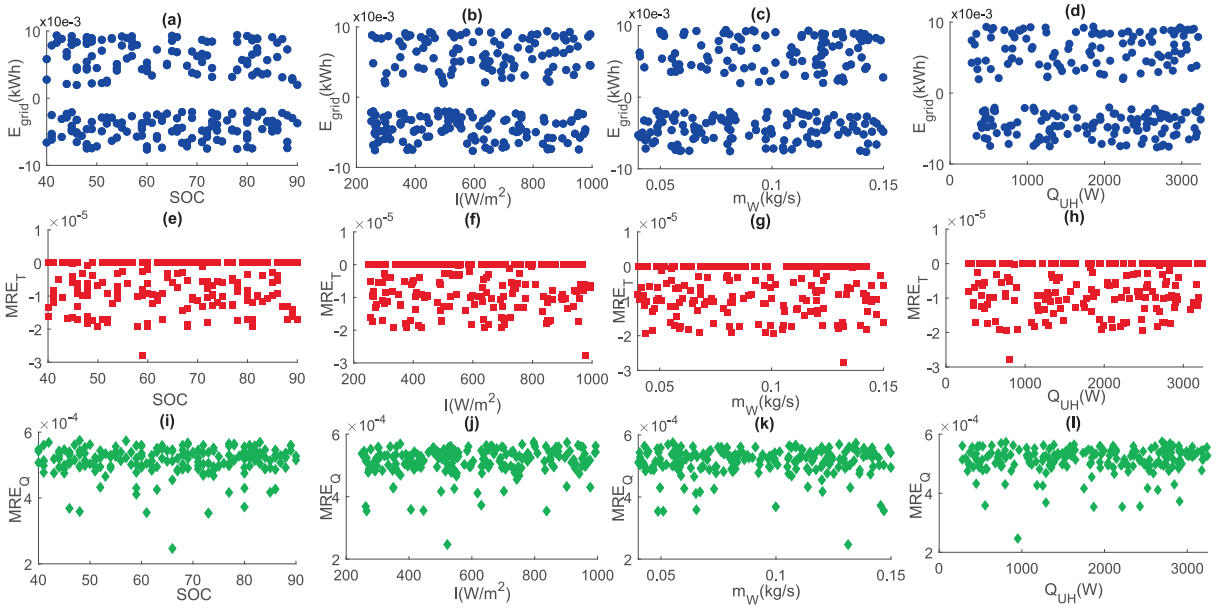

Fig. 9. (a) Sensitivity analysis: (a) E_{GRID} versus SOC, (b) E_{GRID} versus I, (c) E_{GRID} versus m_W and (d) E_{GRID} versus Q_{UH}, (e) MRE_T versus SOC, (f) MRE_T versus I, (g) MRE_T versus m_W and (h) MRE_T versus Q_{UH}, (i) MRE_Q versus SOC, (j) MRE_Q versus I, (k) MRE_Q versus m_W and (l) MRE_Q versus Q_{UH}.

4.3. Hardware in the loop (HIL) experimental validation

This section details the rigorous experimental validation of the proposed EMS and control strategy through a HIL experimental test. To ensure the practical viability and robustness of the proposed framework, this methodology serves as a critical bridge between pure numerical simulation and full-scale physical deployment. In this setup, the entire multi-energy prosumer plant—comprising the dynamic behaviour of both electrical and thermal vectors—is emulated in real-time within the OPAL-RT4512 simulator. Simultaneously, the control logic is hosted on a physical dSPACE MicroLabBox, which acts as the external hardware controller, interacting with the plant through physical analogue and digital I/O channels.

The adoption of HIL experimentation is fundamental in the development of EMS for multi-energy prosumers, as it creates a bidirectional closed-loop environment where the physical controller 'perceives' the emulated thermal and electrical systems as actual hardware. This stage is not merely a real-time simulation exercise but a needed safety protocol in advanced control engineering. It validates the controller's ability to process high-fidelity sensor data and execute control algorithms under strict real-time constraints, accounting for execution times and communication delays that offline simulations cannot capture. Crucially, this approach allows for the stress-testing of the thermal control subsystem under dynamic conditions—such as sudden demand fluctuations—without the inherent risks of component damage, safety hazards, or the prohibitive costs associated with prototyping physical thermal test rigs. Consequently, the HIL platform provides a robust certification of the control architecture's stability before any integration into real-world power systems.

The utility of HIL for validating complex EMS is well-established in recent high-impact literature. For instance, [46] employed HIL to couple substations in real-time with data-driven profiles, analysing thermal prosumer strategies within district heating networks. Similarly, [47] utilised an OPAL-RT OP4512 simulator to validate a model predictive control scheme for energy sharing within a renewable energy community. Addressing the complexity of multi-energy systems, [48] presented a HIL setup based on OPAL-RT to safely test multi-timescale control architectures across different energy domains. Furthermore, [49] validated a FL-EMS for isolated microgrids using an OPAL-RT OP4150 (OP1400 test bench), confirming system stability under steady-state and

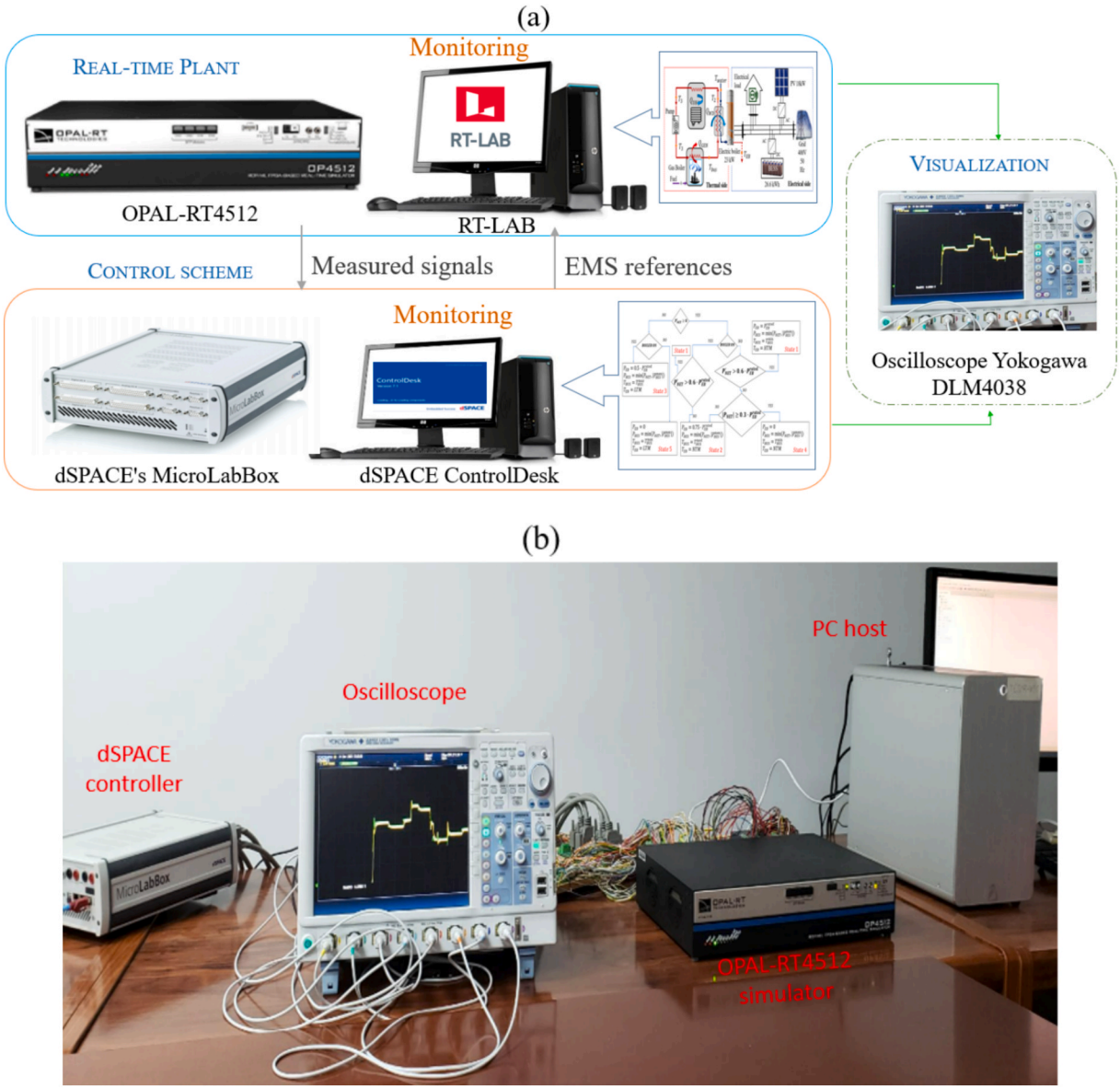

Fig. 10. Experimental HIL setup implemented in the laboratory: (a) Scheme, (b) Photo.

faulty regimes. On the other hand, [50] demonstrated the robustness of a bio-inspired optimization framework by interfacing an OPAL-RT OP5707XG with MATLAB/Simulink R2022b and Raspberry Pi 4B, ensuring real-time coordination for voltage stability and grid resilience.

Regarding the experimental timeframe, the real-time test was explicitly designed to replicate, with high fidelity, the initial 4000 s of the 14,000-second MATLAB/Simulink simulation presented in Section 4.1. This specific duration was strictly defined by the data acquisition capabilities of the high-precision measurement equipment employed. The validation utilised a Yokogawa DLM4038 digital oscilloscope, configured at its maximum time base of 500 s/div, which yields a maximum continuous capture window of 4000 s. This duration allows for the detailed real-time analysis of thousands of control cycles, verifying that the physical controller perfectly tracks the simulated profile.

The architecture of the setup implemented in the laboratory is shown in Fig. 10. The power system is emulated in an OPAL-RT4512 unit, an HIL simulator that enables the real-time implementation and testing of computational models created in MATLAB/Simulink. This unit serves as the emulator of the virtual plant, replicating the fast transient dynamics of the electrical and thermal subsystems with strict numerical stability. The simulator is powered by an Intel® Xeon® E3 v3 4-core processor running at 3.7 GHz and an AMD Kintex™-7 410 T FPGA, which manages the I/O execution with sub-microsecond precision. It is specifically designed for programming using the RT-LAB software, enhancing the ability to simulate and test power system models in real-time.

The control scheme was executed on a dSPACE MicroLabBox, a compact system specifically designed for rapid control prototyping. Acting as the physical controller, this unit reads sensor data and executes the proposed EMS logic using a high-performance quad-core processor. To ensure a synchronized and deterministic interaction, both the plant emulation and the EMS logic were configured with a unified fixed-step sampling time of 0.02 s. The use of a common time base eliminates jitter and ensures that control actions are perfectly aligned with the plant's state updates. The dSPACE MicroLabBox is managed using the ControlDesk software, which facilitates access to model signals for visualization and measurement purposes without additional complexities. Furthermore, the model parameters can be adjusted in real-time without the need to recompile the executable. This setup enables the validation of the findings discussed in Section IV using real-world equipment.

The dSPACE MicroLabBox computes and sends via analog outputs the reference signals, and the OPAL-RT4512 unit receives and operates

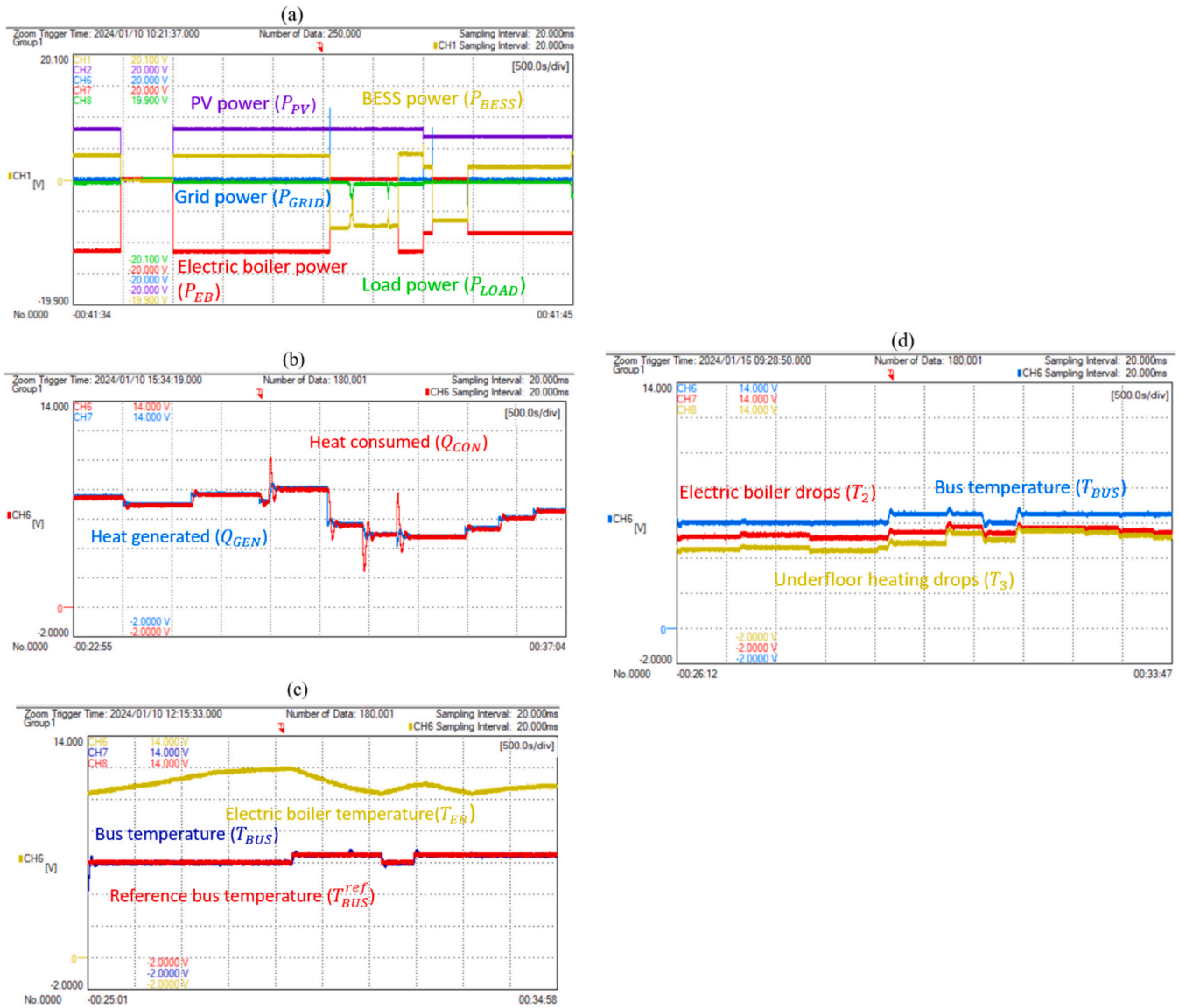

Fig. 11. Experimental results: (a) Electric power balance, (b) Temperature control, (c) Thermal power balance and (d) Temperature drops.

the multi-energy prosumer according to these references. The HIL protocol is established through a high-bandwidth, hardwired analog I/O interface. The cumulative latency of the conversion stages and signal propagation is in the range of 10–20 μs. Given that the control step is 0.02 s, this latency is three orders of magnitude smaller than the system's dynamics and is therefore considered negligible for the stability and accuracy of the multi-energy management. The real-time simulation data is displayed using a Yokogawa DLM4038 oscilloscope, a digital storage oscilloscope employed for precise waveform analysis. The experimental setup scheme and the equipment are shown in Fig. 10a and b. Since the OPAL-RT4512 analog outputs operate within the range of −16 V to +16 V, signals obtained from MATLAB/Simulink must be scaled appropriately for an accurate visualization on the oscilloscope. This scaling procedure serves as the basis for the quantitative evaluation metrics. The validation is grounded in the metrological calibration of the oscilloscope's vertical (Volts/division) and horizontal (seconds/division) scales, using linear conversion to correlate the −16/+16 V range with physical units (e.g., kW, °C). The accuracy was verified through the mathematical concordance between the captured voltage levels and the theoretical setpoints, providing a rigorous quantitative verification of the EMS performance under real-time operation.

A real-time simulation with a duration of 4000 s was conducted. The electrical energy balance is shown in Fig. 11a. For a clear visualisation, a time scale of 500 s/div and a signal scale of 5 V/div were selected. The signal measurements in MATLAB/Simulink were initially divided by 2000 and then displayed on the oscilloscope. For instance, P_{PV} (purple signal) has a value of 16.2 kW at the beginning of the Simulink simulation (Fig. 6a). When divided by 2000 and displayed on a 5 V/div scale, this corresponds to 8.1 V, which is consistent with the applied scaling.

Fig. 11a also shows P_{BESS} (yellow trace), P_{GRID} (blue trace), P_{LOAD} (green trace) and P_{EB} (red trace). The behaviour of these traces in the figure clearly shows the change in operation mode of the multi-energy prosumer from HTM to NTM. This is evident from the change in the consumption of the electric boiler, which shifts from 23 kW (−11.5 V) to 17.25 kW (−8.6 V). Furthermore, zero grid consumption is maintained demonstrating the effective response of the BESS in compensating for fluctuations in the electric load.

The thermal balance is depicted in Fig. 11b. Similar to the electrical balance, a time scale of 500 s/div and a signal scale of 2 V/div were chosen. In this case, the signals were initially divided by 1000. The figure shows the heat flow injected by the gas boiler (blue trace) and the heat flow consumed (red trace). At the beginning of the simulation, the gas boiler delivers 7.5 kW (Fig. 7a); therefore, when divided by 1000 and scaled down to 2 V/div, a signal of 7.5 V should result.

The temperature control is depicted in Fig. 11c. The same time scale and signal scale as described above were chosen. In this case, the signals derived from Simulink were divided by 5. The output temperature of the electric boiler (yellow trace), the measured bus temperature (blue trace), and the reference bus temperature (red trace) are shown. To visualise the representation, the bus temperature takes a value of 30 °C in HTM. Therefore, with the scaling applied, 6 V are measured for the bus temperature, which confirms the results shown in Fig. 8a. This behaviour also demonstrates the transition of the multi-energy prosumer from HTM to NTM, as evidenced by the shifts in the electric boiler temperature and the bus temperature. For instance, the thermal bus shifts from 30 °C (6 V) to 32.5 °C (6.5 V).

Finally, Fig. 11d shows the temperature drops using the same scales as before. The signal values are also divided by 5. The measured bus temperature (blue trace), temperature drops in the electric boiler exchange (red trace), and temperature drop in the underfloor heating exchange (yellow trace) are shown. As seen, the results confirm that T_{bus} is higher than T_2 and T_2 is also higher than T_3, which is consistent with the behavior exhibited in Fig. 8b.

In summary, the experimental results presented in this section are consistent with the MATLAB/Simulink analysis conducted in Section 4.1, thus verifying the effectiveness of the control scheme and the efficacy of the state-based EMS.

4.4. Long-time comparison against fuzzy-logic EMS

To further validate the performance and robustness of the proposed state-based EMS, this section provides a comparative analysis against a high-fidelity benchmark fuzzy logic-based EMS (FL-EMS) over a 24-h dynamic study horizon. The FL-EMS has been carefully refined to ensure a rigorous and fair benchmarking process, resulting in an accurate balance between control precision and computational load. Crucially, to improve the simulation runtime, a multi-rate execution strategy was implemented. While the dynamic multi-energy model of the prosumer operates at a high temporal resolution (T_s = 0.02 s) to capture dynamic transients, the FL-EMS decision-making frequency was decoupled and set to 0.1 s. This approach respects the slower thermal dynamics of the system while significantly lowering the computational requirements compared to a fully coupled simulation.

To this end, the fuzzy controller operates using two primary input signals: the available PV power (P_{PV}) and the total electrical demand (P_{LOAD}). The fundamental objective of the FL-EMS is congruent with that of the proposed state-based scheme: to determine the appropriate reference temperature for the gas boiler (T_{bus}^{ref}), the upper hysteresis threshold for the electric boiler (T_{EB}^{max}), and the electric boiler power consumption (T_{EB}).

The design of the membership functions is illustrated in Fig. 12. To reduce the arithmetic complexity per inference cycle, all MFs have been modelled utilizing exclusively triangular and trapezoidal geometries, avoiding computationally demanding Gaussian functions. Specifically, the P_{PV} input (Fig. 12a) is discretised into five distinct linguistic levels: very low (VL), low (L), medium (M), high (H), and very high (VH), enabling precise energy distribution decisions. Similarly, the P_{LOAD} input (Fig. 12b) is categorised into low (L), normal (N), and high (H) demand states. The cross-combination of these input variables results in a rule base comprising 15 possible operational configurations.

Regarding the output variables, Fig. 12c depicts the configured low (L), medium (M), and high (H) membership functions for the T_{GB} control, while Fig. 12d and e represents the L, N, and H functions for the electric boiler's power consumption and its hysteresis shutdown temperature, respectively. The heuristic logic governing the FL-EMS is predicated on prioritising renewable surplus to drive the electric boiler at high temperatures and full power consumption. As renewable resource availability declines, the electric boiler's demand is systematically throttled and primarily sustained by the BESS, provided sufficient capacity is available. The complete set of fuzzy rules covering the entire operational spectrum is detailed in Table 6.

Fig. 13 illustrates the dynamic response of both control systems over a dynamic 24-h horizon, with Fig. 13a representing the proposed state-based EMS and Fig. 13b depicting the FL-EMS benchmark. To contextualise these profiles, the input variables exhibit characteristic daily trajectories that drive the system's logic. The renewable resource (P_{PV}) production starts at t = 7h and reaches a peak generation of 18 kW at t = 14.5 h before ceasing at t = 20 h. Simultaneously, the prosumer electrical demand (P_{LOAD}) displays a highly stochastic and intermittent nature; with significant demand peaks of −13 kW occurring around midday (t = 13 h). These fluctuating signals necessitate a robust management strategy to prioritise multi-energy loads whilst managing renewable volatility. Following the established sign convention, positive values for P_{GRID} denote power injection into the primary grid (export), whilst negative values indicate power import (consumption).

The operational divergence begins during the morning ramp (t = 6–10 h). As P_{PV} commences its ascent, both controllers activate the electric boiler. However, the proposed EMS maintains a disciplined setpoint dynamically matched to the available renewable surplus, reaching a modulated consumption of approximately 15 kW. In contrast, the FL-EMS exhibits a discrete, step-like behaviour, with P_{EB} settling at a

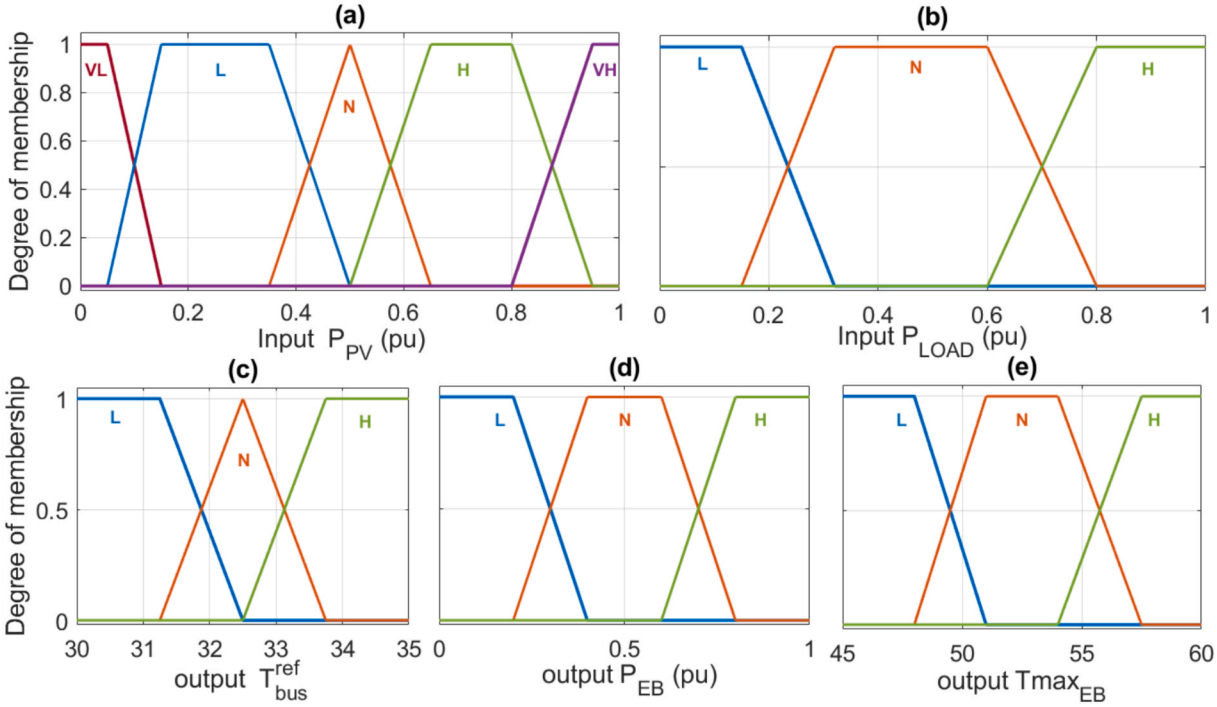

Fig. 12. Membership functions: (a) PV power (P_{PV}), (b) electrical demand (P_{LOAD}), (c) temperature in the thermal bus (T_{bus}), (d) electric boiler power (P_{EB}), (e) temperature in the thermal bus (T_{bus}).

Table 6
FL-EMS inference rules.

P_{PV} (input)	P_{LOAD} (input)	T^{ref}_{bus} (output)	P_{EB} (output)	T^{max}_{EB} (output)
VL	L	H	N	L
VL	N	H	L	L
VL	H	H	L	L
L	L	N	N	N
L	N	N	L	N
L	H	H	L	L
M	L	L	H	H
M	N	N	N	N
M	H	H	N	N
H	L	L	H	H
H	N	L	H	H
H	H	N	N	H
VH	L	L	H	H
VH	N	L	H	H
VH	H	L	H	H

fixed intermediate level of approximately 12.5 kW early in the day. Notably, the fuzzy controller sustains this operation for a more prolonged duration, resulting in a broader activation window compared to the proposed scheme.

At the central hours of the day (t = 12–16 h), the difference in control performance becomes even more apparent. In the proposed EMS (Fig. 13a), the electric boiler operation is regulated to a modulated capacity of roughly 15 kW, allowing for a less BESS discharging operation. Conversely, the FL-EMS (Fig. 13b) responds to the peak solar irradiance states by driving the actuator to its full rated power. Consequently, the P_{EB} profile is characterised by intensified fluctuations and higher peaks (exceeding 20 kW). Although both controllers manage to export power during peak irradiance, the proposed controller ensures a smoother operation of the electric boiler, preventing excessive thermal cycling and mechanical wear.

The most decisive technical advantage occurs during the evening peak (t = 18–22 h). As P_{PV} production ceases, the proposed state-based EMS triggers a strategic BESS discharge phase that successfully covers the entirety of the domestic demand and thermal requirements for the majority of the interval. This strategy ensures that P_{GRID} remains at 0 kW for an extended period, delaying grid dependency until the storage is fully exhausted. A pivotal divergence is observed in the FL-EMS (Fig. 13b), where the controller exhibits grid dependency at two critical intervals. Firstly, during the morning ramp (t = 8–10 h), the specific rule configuration necessitates an import of approximately −10 kW from the primary grid to sustain the boiler's activation. Subsequently, a second and more pronounced period of dependency occurs during the night. Due to a less optimised discharge profile earlier in the day, the storage capacity is depleted by t = 20 h, leaving the system without reserves to cover the simultaneous loads. This is evidenced at t = 21 h, where the FL-EMS reaches a peak power import of −16 kW. In contrast, although the state-based logic (Fig. 13a) also eventually resorts to the grid upon BESS depletion, this event is delayed until t > 21 h and results in a lower peak import of approximately −13 kW, effectively shielding the prosumer from the higher level of grid dependency observed in the benchmark.

Quantitatively, these operational refinements lead to a superior energy balance. The proposed architecture achieves a substantial 36.31% reduction in total grid energy import compared to the fuzzy logic benchmark. Furthermore, the more rationalised use of the electric boiler—avoiding the high-power bursts seen in the FL-EMS—optimises the thermal vector, resulting in a 2.23% saving in the electric boiler's energy consumption. These results confirm that the proposed state-based EMS provides a significantly more robust, deterministic, and efficient solution for multi-energy prosumers than traditional heuristic methods.

The thermal impact of the management strategies is evaluated through the temperature profiles of the electric boiler and the thermal bus as depicted in Fig. 14. These profiles illustrate how the electrical control actions discussed in the previous section translate into thermal energy storage and delivery. In both scenarios, the temperature regulation is intrinsically coupled with PV production, utilising renewable surplus to maintain the system's thermal state.

The proposed state-based EMS (Fig. 14a) maintains a consistently

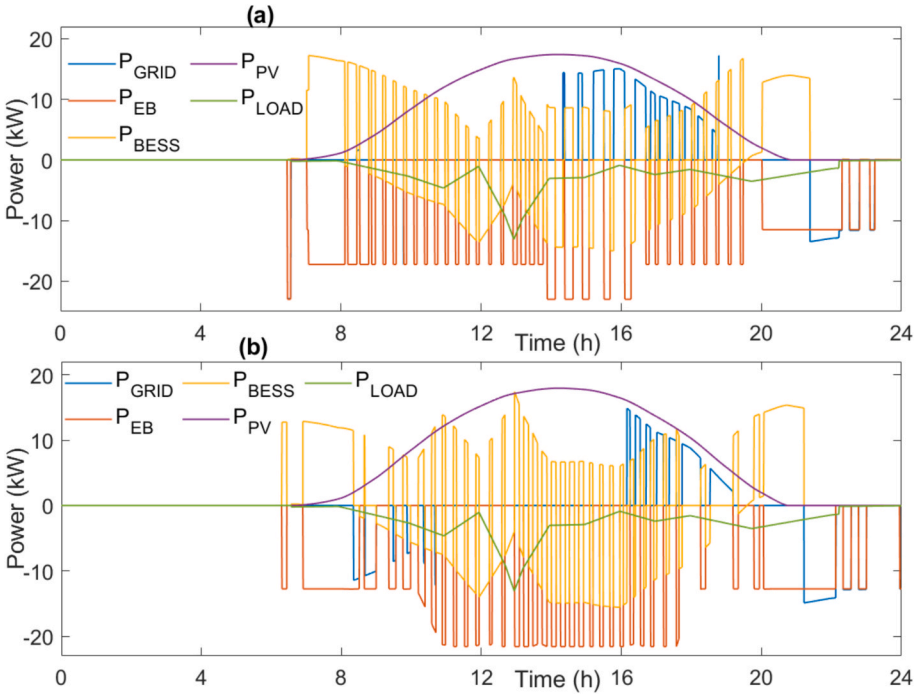

Fig. 13. Electric power balance for the multi-energy prosumer: (a) state-based EMS and (b) FL-EMS.

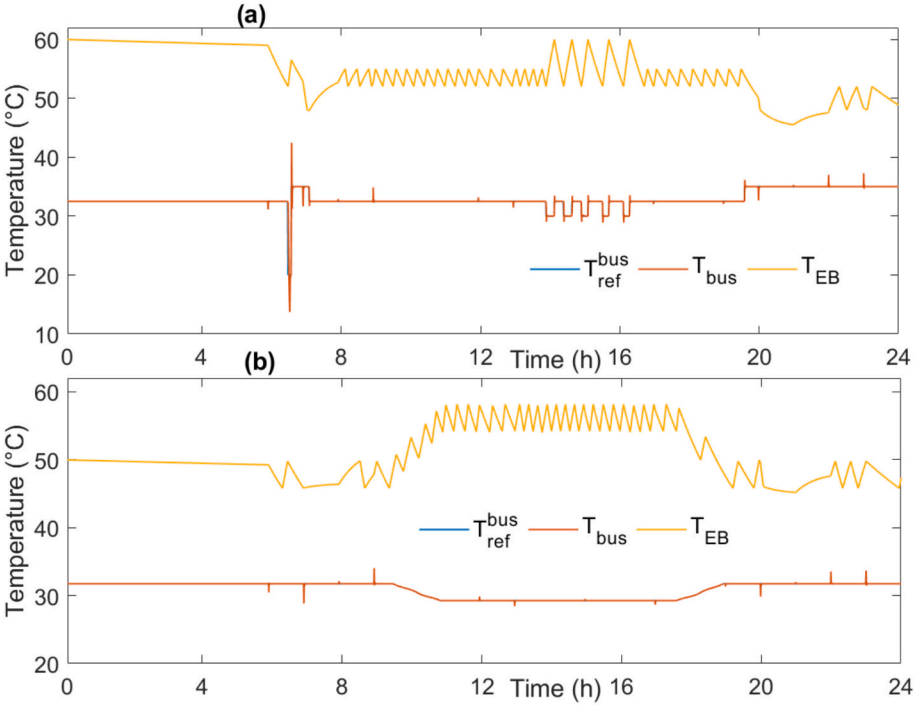

Fig. 14. Temperature control for the multi-energy prosumer: (a) states-based EMS and (b) FL-EMS.

higher thermal grade throughout the 24-h cycle. Quantitatively, the proposed controller achieves a mean electric boiler temperature of 54.33 °C, compared to 50.86 °C in the FL-EMS (Fig. 14b). This higher average value in T_{EB} signifies a more robust thermal buffer, effectively storing renewable-origin energy to meet the prosumer's heating demands. The superiority of the proposed logic is most evident in the thermal bus temperature, which serves as the primary interface for the gas boiler. Under the proposed EMS, T_{bus} is maintained at a mean value of 32.79 °C, significantly higher than the 30.9 °C observed in the FL-EMS. This increased temperature in the thermal bus acts as a "renewable pre-heating" stage. By sustaining a higher baseline temperature via the electric boiler's renewable contribution, therefore reducing the electric boiler consumption.

Beyond the energy and thermal advantages previously discussed, the technical robustness of the control level was evaluated using the MRE for temperature tracking (MRE_T) and heating power delivery (MRE_Q). As evidenced in the numerical results, the tracking performance of both the proposed state-based EMS and the FL-EMS benchmark is remarkably

high, with error values practically negligible and close to zero. Specifically, for the proposed framework, the average MRE_T is $4.72{\cdot}10^{-6}$ and MRE_Q is $4.74{\cdot}10^{-4}$. For the case of the FL-EMS, these metrics were $7.14{\cdot}10^{-6}$ and $4.20{\cdot}10^{-4}$, respectively. These indexes confirm that both controllers are equally capable of following their internal setpoints with high fidelity, ensuring that the observed energy savings are the result of superior strategy rather than mere differences in tracking accuracy.

However, a marked contrast becomes evident upon assessing the computational overhead necessary to generate these findings. The simulation-based validation was performed using MATLAB/Simulink (R2024b) on a dedicated hardware configuration comprising an AMD Ryzen 7 7700 8-core CPU (4.50 GHz) and 64 GB of RAM, under a Windows 11 Enterprise operating system. The proposed state-based EMS completed the full 24-h dynamic simulation in a remarkable 1 min. In stark contrast, the heuristic complexity of the FL-EMS extended the simulation time to 30 min. This represents a massive 30-fold reduction in computational burden.

To rigorously justify this performance gap, it is necessary to contrast the arithmetic operations executed by each controller per simulation time-step. The proposed rule-based flowchart operates as a deterministic decision tree with a maximum logical depth of four nodes. Even in the most complex execution path, the processor is required to evaluate roughly four relational comparisons (e.g., checking net power flow or boiler status). Consequently, the computational burden is strictly limited to a sequence of elementary Boolean checks, which entails negligible processing consumption.

In a marked contrast, the FL-EMS imposes a substantial arithmetic penalty due to the defuzzification process required for its three simultaneous outputs (T_{bus}^{ref}, P_{EB}, T_{EB}^{max}). To resolve these variables using the standard centre of gravity method within a discrete simulation environment of 101 points, the solver cannot simply select a pre-defined state; it must numerically integrate the area under the curve. Mathematically, this forces the simulation engine to execute a calculation loop of 303 specific arithmetic iterations (three output variables multiplied by 101 integration points) during every single time-step, necessitating continuous multiplication and cumulative summation routines. It is this compounding effect—multiplying this heavy arithmetic load by the vast number of simulation steps—that physically results in the observed 30-fold increase in execution time, validating the flowchart as the superior solution for time-efficient energy management.

The comparative results confirm that the proposed state-based EMS outperforms the FL-EMS benchmark by reducing electric boiler and primary grid energy consumption while ensuring superior thermal indices. Crucially, while both architectures deliver nearly ideal control precision with MRE indices effectively approaching zero, the proposed framework achieves this performance with a 30-fold reduction in computational cost—completing the 24-h cycle in 1 min compared to the 30 min required by the fuzzy logic inference. This unique synergy of high-fidelity tracking, enhanced energy efficiency, and minimal processing overhead establishes the proposed deterministic scheme as a significantly more robust and scalable solution for real-time multi-energy management in prosumer environments. Table 7 summarised the comparison of the state-based EMS against the FL-EMS.

Table 7
Comparison of state-based EMS vs FL-EMS.

	States-based EMS	FL-EMS	Variation (%)
E_{GRID}^{tot} (kWh)	16.79	26.48	−36.61
E_{GB}^{tot} (kWh)	125	128.4	−2.23
MRE_T (°C)	$4.72{\cdot}10^{-6}$	$7.14{\cdot}10^{-6}$	–
MRE_Q (W)	$4.74{\cdot}10^{-4}$	$4.20{\cdot}10^{-4}$	–
Computational cost (min)	1	30	–

5. Conclusions

This paper presented the dynamic modelling and control of a multi-energy prosumer comprising heat and electricity vectors. The dynamic coordination between thermal and electrical sources was achieved through a novel state-based EMS—aimed at avoiding reliance on the local grid to supply energy demand. This design was rooted in a dimensionless philosophy using normalised thresholds and ratios, which allowed the control logic to remain agnostic to building scales and climatic conditions. By basing the decision-making process on generic, easily measurable variables, such as net and gross power, the strategy ensured its applicability across diverse multi-energy infrastructures. Furthermore, the control architecture was designed with intrinsic scalability features. The established nodal structure of the thermal network provides a modular foundation for the inclusion of new components, while the three-phase electrical framework supports the parallel integration of additional energy assets. The low computational footprint of the logic, verified in the successfully real-time HIL execution, evidenced that the control is well-suited for larger prosumer clusters, as it can be deployed without incurring significant computational overhead.

The implementation of three distinct operating states, namely HTM, NTM and LTM, enables an effective synchronisation between the heat and electricity vectors. The surplus renewable energy available in the system is a key parameter to manage the multi-energy prosumer operating modes. The electricity vector assumed the primary role as energy carrier in meeting energy demands, leading to reduce gas consumption in high renewable energy scenarios. However, when renewable energy diminished, electrical requirements were safeguarded, and the electric boiler reduced its consumption. The gas boiler increased the temperature of the thermal bus to decrease the electric boiler consumption. The effectiveness of the dynamic control scheme was verified through three different analyses, encompassing several operating conditions, including variations in weather and peak thermal and electrical loads. The efficacy and robustness of the dynamic control scheme under diverse and challenging operating conditions were probed under a comprehensive sensitivity analysis involving 250 simulations.

The findings indicated an average electrical energy consumption of 4.554×10^{-6} kWh for the local grid, demonstrating minimal reliance on it. Additionally, the thermal bus control exhibited an average MRE of 8.375×10^{-6} °C and the thermal balance control an MRE of 5.12×10^{-4} W, indicating precise temperature control.

To further validate the findings under real-world conditions, an experimental HIL test was conducted using an OPAL-RT4512 and a dSPACE MicroLabBox control unit. The 4000-second real-time experiment successfully replicated the simulation results with actual equipment, confirming the practical applicability of the proposed control scheme and EMS. Beyond its functional success, the system demonstrated high potential for scalability. The established nodal architecture of the thermal network is designed to allow the seamless inclusion of new components, while the three-phase electrical framework facilitated the parallel integration of additional energy assets. Finally, the low computational footprint of the control scheme, verified during the real-time HIL execution, confirmed its suitability for industrial-grade controllers and larger prosumer clusters without significant computational overhead.

Within a 24-h dynamic operational scenario, the proposed state-based EMS demonstrated marked superiority over the fuzzy logic benchmark, achieving a 36.61% reduction in grid dependency and a 2.23% saving in auxiliary fuel consumption through enhanced multi-energy coordination. Furthermore, the proposed architecture yielded a massive 30-fold reduction in computational time while maintaining MRE index effectively negligible and virtually zero for both control schemes. Consequently, these results established the proposed framework as a significantly more efficient and scalable solution for real-time energy management than traditional heuristic approaches.

CRediT authorship contribution statement

Pablo Horrillo-Quintero: Writing – original draft, Visualization, Validation, Software, Resources, Methodology, Investigation, Formal analysis, Data curation, Conceptualization. **Pablo García-Triviño:** Writing – original draft, Visualization, Validation, Software, Resources, Methodology, Investigation, Formal analysis, Conceptualization. **Carlos E. Ugalde-Loo:** Writing – review & editing, Methodology, Investigation, Formal analysis, Conceptualization. **David Carrasco-González:** Writing – original draft, Visualization, Validation, Software, Resources, Methodology, Investigation, Formal analysis, Conceptualization. **Vedran Peric:** Writing – review & editing, Methodology, Investigation, Conceptualization. **Luis M. Fernández-Ramírez:** Writing – review & editing, Writing – original draft, Visualization, Validation, Supervision, Project administration, Methodology, Investigation, Funding acquisition, Formal analysis, Conceptualization.

Declaration of competing interest

The authors declare that they have no known competing financial interests or personal relationships that could have influenced the work reported in this study.

Acknowledgment

This work was support in part by the Consejería de Universidades, Investigación e Innovación de la Junta de Andalucía (Grant DGP_PIDI_2024_02368) and by the Ministerio de Ciencia, Innovación y Universidades, Agencia Estatal de Investigación, FEDER, UE (Grant PID2024-156036OB-C32 supported by MCIN /AEI /10.13039/501100011033 /FEDER, UE).

Data availability

Data will be made available on request.

References

[1] Y. Wang, L. Han, X. Deng, H. Gao, Optimization scheduling of household integrated energy systems for improving thermal comfort with low cost, Energy Build. 329 (2025), https://doi.org/10.1016/j.enbuild.2024.115229.
[2] M. Tostado-Véliz, P. Arévalo, F. Jurado, A comprehensive electrical-gas-hydrogen Microgrid model for energy management applications, Energy Convers. Manag. 228 (2021), https://doi.org/10.1016/j.enconman.2020.113726.
[3] E. Guelpa, A. Bischi, V. Verda, M. Chertkov, H. Lund, Towards future infrastructures for sustainable multi-energy systems: a review, Energy 184 (2019) 2–21, https://doi.org/10.1016/j.energy.2019.05.057.
[4] J. Zhong, Y. Li, Y. Wu, Y. Cao, Z. Li, Y. Peng, et al., Optimal operation of energy hub: an integrated model combined distributionally robust optimization method with Stackelberg game, IEEE Trans. Sustain. Energy 14 (2023) 1835–1848, https://doi.org/10.1109/TSTE.2023.3252519.
[5] L. Tian, L. Cheng, J. Guo, K. Wu, System modeling and optimal dispatching of multi-energy microgrid with energy storage, J. Mod Power Syst. Clean Energy 8 (2020) 809–819, https://doi.org/10.35833/MPCE.2020.000118.
[6] Y. Jiang, C. Wan, C. Chen, M. Shahidehpour, Y. Song, A hybrid stochastic-interval operation strategy for multi-energy microgrids, IEEE Trans. Smart Grid 11 (2020) 440–456, https://doi.org/10.1109/TSG.2019.2923984.
[7] Y. Sang, J. Li, P. Li, Z. Wang, Z. Wan, J. Jurasz, et al., Study on optimization and risk resilience of integrated energy system in near-zero carbon park considering carbon taxes, Energy Build. 335 (2025), https://doi.org/10.1016/j.enbuild.2025.115578.
[8] Z. Li, J. Zhou, J. Wen, X. Chen, Dynamic modeling and operations of a heat-power station system based on renewable energy, CSEE J. Power Energy Syst 8 (2022) 1110–1121, https://doi.org/10.17775/CSEEJPES.2020.03470.
[9] X. Lei, Y. Lin, Q. Yang, J. Zhou, X. Chen, J. Wen, Research on coordinated control of renewable-energy-based Heat-Power station system, Appl. Energy 324 (2022), https://doi.org/10.1016/j.apenergy.2022.119736.
[10] Y. Gao, L. Huang, C. Yun, Y. Zhang, Research on low carbon economic dispatch of integrated energy system based on source-grid-load-storage collaboration, Energy Build. (2025) 116434, https://doi.org/10.1016/j.enbuild.2025.116434.
[11] G. Comodi, A. Bartolini, F. Carducci, B. Nagaranjan, A. Romagnoli, Achieving low carbon local energy communities in hot climates by exploiting networks synergies in multi energy systems, Appl. Energy 256 (2019), https://doi.org/10.1016/j.apenergy.2019.113901.
[12] Y. Lei, X. Chen, K. Jiang, H. Li, Z. Zou, A novel methodology for electric-thermal mixed power flow simulation and transmission loss analysis in multi-energy microgrids, Front. Energy Res. 8 (2021), https://doi.org/10.3389/fenrg.2020.620259.
[13] N. Holjevac, T. Capuder, I. Kuzle, N. Zhang, C. Kang, Modelling aspects of flexible multi-energy microgrids, in: Power Systems Computation Conference (PSCC) Dublin, Ireland 2018, 2018, pp. 1–7, https://doi.org/10.23919/PSCC.2018.8442468.
[14] D. Xu, B. Zhou, K.W. Chan, C. Li, Q. Wu, B. Chen, et al., Distributed multienergy coordination of multimicrogrids with biogas-solar-wind renewables, IEEE Trans. Ind. Inform. 15 (2019) 3254–3266, https://doi.org/10.1109/TII.2018.2877143.
[15] C. Zhang, Y. Xu, Z.Y. Dong, L.F. Yang, Multitimescale coordinated adaptive robust operation for industrial multienergy microgrids with load allocation, IEEE Trans. Ind. Inform. 16 (2020) 3051–3063, https://doi.org/10.1109/TII.2019.2907710.
[16] D. Qiu, T. Chen, G. Strbac, S. Bu, Coordination for multienergy microgrids using multiagent reinforcement learning, IEEE Trans. Ind. Inform. 19 (2023) 5689–5700, https://doi.org/10.1109/TII.2022.3168319.
[17] S.R. Seyednouri, A. Safari, M. Farrokhifar, S.N. Ravadanegh, A. Quteishat, M. Younis, Optimal stochastic scheduling of a multi-carrier multi-microgrid system considering storages, demand responses, and thermal comfort, Sustain. Cities Soc. 99 (2023), https://doi.org/10.1016/j.scs.2023.104943.
[18] Y. Liu, F. Zhang, K. Sun, G. Wu, Economic operation of CCHP microgrid with heat pump and energy storage, in: 2023 IEEE IAS Industrial and Commercial Power System Asia, I and CPS Asia 2023, Institute of Electrical and Electronics Engineers Inc., 2023, pp. 1071–1075, https://doi.org/10.1109/ICPSAsia58343.2023.10294883.
[19] B.J. Tang, X.L. Cao, R. Li, Z.B. Xiang, S. Zhang, Economic and low-carbon planning for interconnected integrated energy systems considering emerging technologies and future development trends, Energy 302 (2024), https://doi.org/10.1016/j.energy.2024.131850.
[20] H. Chen, S. Yang, J. Chen, X. Wang, Y. Li, S. Shui, et al., Low-carbon environment-friendly economic optimal scheduling of multi-energy microgrid with integrated demand response considering waste heat utilization, J. Clean. Prod. 450 (2024), https://doi.org/10.1016/j.jclepro.2024.141415.
[21] C. Yang, X. Dong, G. Wang, D. Lv, R. Gu, Y. Lei, Low-carbon economic dispatch of integrated energy system with CCS-P2G-CHP, Energy Rep. 12 (2024) 42–51, https://doi.org/10.1016/j.egyr.2024.05.055.
[22] B. Kilkis, Optimum utilization of power plant waste heat by nearly-zero exergy district prosumers for minimum carbon footprint, Smart Energy 20 (2025), https://doi.org/10.1016/j.segy.2025.100204.
[23] Y. Fu, J. Shan, Z. Li, B.L. Xie, J.S. Pan, The optimal bidding strategy for multi-energy prosumers in the double auction electricity-heat market: a bidding space model, Energy 314 (2025), https://doi.org/10.1016/j.energy.2024.134167.
[24] J. Stolarski, E. Olba-Zięty, M.J. Stolarski, Economic analysis of renewable energy generation from a multi-energy installation in a single-family house, Energies (Basel) 17 (2024), https://doi.org/10.3390/en17246213.
[25] K. Ikuta, H. Aki, Multi-timescale management models for distributed energy resources and a two-stage incentive design for demand-side grid flexibility provision, Sustain. Energy Grids Networks 41 (2025), https://doi.org/10.1016/j.segan.2024.101618.
[26] J. Yu, L. Guo, M. Ma, S. Kamel, W. Li, X. Song, Risk assessment of integrated electrical, natural gas and district heating systems considering solar thermal CHP plants and electric boilers, Int. J. Electr. Power Energy Syst. 103 (2018) 277–287, https://doi.org/10.1016/j.ijepes.2018.06.009.
[27] Y. Noorollahi, R. Zahedi, E. Ahmadi, A. Khaledi, Low carbon solar-based sustainable energy system planning for residential buildings, Renew. Sustain. Energy Rev. 207 (2025), https://doi.org/10.1016/j.rser.2024.114942.
[28] S. Heinen, D. Burke, M. O'Malley, Electricity, gas, heat integration via residential hybrid heating technologies – an investment model assessment, Energy 109 (2016) 906–919, https://doi.org/10.1016/j.energy.2016.04.126.
[29] K. Hu, L. Lu, Q. Yang, Y. Feng, B. Wang, Multi-objective optimization of electric–gas–thermal systems via the hippo optimization algorithm: low-carbon and cost-effective solutions, Sustainability (Switzerland) 17 (2025), https://doi.org/10.3390/su17229970.
[30] CARNOT Toolbox for Matlab/Simulink R2022a, © Solar-Institut Jülich; n.d. Online Available: https://www.fh-aachen.de/en/research/institutes/sij/equipment/carnot-toolbox.
[31] S. Lohmann, Einführung in die Software MATLAB® - Simulink® und die Toolboxen CARNOT und Stateflow® zur Simulation von Gebäude- und Heizungstechnik.
[32] L. Pompei, J. Mannhardt, F. Nardecchia, L.M. Pastore, L. de Santoli, A Different approach to develop a district heating grid based on the optimization of building clusters, Processes 10 (2022), https://doi.org/10.3390/pr10081575.
[33] H.I. Ben, D. Pietruschka, Hardware-in-the-loop test for a parabolic trough collector plant in the meat industry, in: Energy Procedia, vol. 91, Elsevier Ltd, 2016, pp. 585–590, https://doi.org/10.1016/j.egypro.2016.06.206.
[34] R. Meligy, M. Rady, A. El Samahy, A. Montenon, W. Mohamed, Hierarchical control of multi-generation solar thermal power plant, Appl. Therm. Eng. 222 (2023), https://doi.org/10.1016/j.applthermaleng.2022.119942.
[35] P. Hua, H. Wang, Z. Xie, R. Lahdelma, Integrated demand response method for heating multiple rooms based on fuzzy logic considering dynamic price, Energy 307 (2024), https://doi.org/10.1016/j.energy.2024.132577.
[36] G. Salvadori, L. Ferrari, L. Romano, F. Fantozzi, Use of CARNOT toolbox to evaluate the impact of building automation and control systems on energy and CO2 emission savings, in: 2020 IEEE International Conference on Environment and Electrical Engineering and 2020 IEEE Industrial and Commercial Power Systems Europe (EEEIC/I&CPS Europe), Madrid, Spain, 2020, pp. 1–6, https://doi.org/10.1109/EEEIC/ICPSEurope49358.2020.9160742.

[37] W. De Soto, S.A. Klein, W.A. Beckman, Improvement and validation of a model for photovoltaic array performance, Sol. Energy 80 (1) (2006) 78–88, https://doi.org/10.1016/j.solener.2005.06.010.
[38] B. Yang, J. Wang, X. Zhang, T. Yu, W. Yao, H. Shu, et al., Comprehensive overview of meta-heuristic algorithm applications on PV cell parameter identification, Energy Convers. Manag. 208 (2020), https://doi.org/10.1016/j.enconman.2020.112595.
[39] Hydro-Quebec and The MathWorks, Inc., SimPowerSystemsTM. Reference, Hydro-Quebec and The MathWorks, Inc., Natick, MA, 2015. https://www.mathworks.com/help/sps/index.html.
[40] A. Dini, S. Pirouzi, M. Norouzi, M. Lehtonen, Grid-connected energy hubs in the coordinated multi-energy management based on day-ahead market framework, Energy 188 (2019), https://doi.org/10.1016/j.energy.2019.116055.
[41] M. Rose, C.A. Hans, J. Schiffer, A predictive operation controller for an electro-thermal microgrid utilizing variable flow temperatures, in: IFAC-PapersOnLine, vol. 56, Elsevier B.V., 2023, pp. 5444–5450, https://doi.org/10.1016/j.ifacol.2023.10.195.
[42] T.M. Alabi, L. Lu, Z. Yang, Real-time automatic control of multi-energy system for smart district community: a coupling ensemble prediction model and safe deep reinforcement learning, Energy 304 (2024), https://doi.org/10.1016/j.energy.2024.132209.
[43] S. Chapaloglou, A. Nesiadis, K. Atsonios, N. Nikolopoulos, P. Grammelis, A. Carrera, et al., Microgrid energy management strategies assessment through coupled thermal-electric considerations, Energy Convers. Manag. 228 (2021), https://doi.org/10.1016/j.enconman.2020.113711.
[44] H. Cui, W. Xia, S. Yang, X. Wang, Real-time emergency demand response strategy for optimal load dispatch of heat and power micro-grids, Int. J. Electr. Power Energy Syst. 121 (2020), https://doi.org/10.1016/j.ijepes.2020.106127.
[45] Z. Liu, G. Fan, X. Meng, Y. Hu, D. Wu, G. Jin, et al., Multi-time scale operation optimization for a near-zero energy community energy system combined with electricity-heat-hydrogen storage, Energy 291 (2024), https://doi.org/10.1016/j.energy.2024.130397.
[46] P. Sdringola, M. Pipiciello, M. Ricci, F. Gianaroli, D. Menegon, F. Trentin, et al., Prosumers and district heating: experimental validation of strategies to improve thermal energy production and consumption, Energy Build. 338 (2025), https://doi.org/10.1016/j.enbuild.2025.115713.
[47] C. Rodio, A. Sagripanti, R. Lazzari, Control hardware-in-the-loop assessment of an energy management system for renewable energy communities, in: Conference Proceedings – 2025 IEEE International Conference on Environment and Electrical Engineering and 2025 IEEE Industrial and Commercial Power Systems Europe, EEEIC/I and CPS Europe 2025, Institute of Electrical and Electronics Engineers Inc., 2025, https://doi.org/10.1109/EEEIC/ICPSEurope64998.2025.11169049.
[48] D. Liu, E. De Din, D. Carta, A. Benigni, Controller hardware-in-the-loop testing of a multitimescale control architecture for multienergy systems, IEEE J. Emerg. Sel. Top. Ind. Electron. 6 (2025) 499–510, https://doi.org/10.1109/JESTIE.2025.3546680.
[49] A. El Zerk, M. Ouassaid, Real-time fuzzy logic based energy management system for microgrid using hardware in the loop, Energies (Basel) 16 (2023), https://doi.org/10.3390/en16052244.
[50] A. Boukaibat, N. Krami, Y. Rochdi, Y. El Bakkali, M. Laamim, A. Rochd, Real-time energy management in microgrids: integrating T-cell optimization, droop control, and HIL validation with OPAL-RT, Energies (Basel) 18 (2025), https://doi.org/10.3390/en18154035.